

# A Radio Spectral Line Study of the 2-Jy IRAS-NVSS Sample: Part I

Maria Ximena Fernandez

*Department of Astronomy, Columbia University, 550 West 120th Street, New York, NY  
10027*

ximena@astro.columbia.edu

Emmanuel Momjian

*National Radio Astronomy Observatory, P. O. Box O, Socorro, NM, 87801*

emomjian@nrao.edu

Christopher J. Salter

*NAIC, Arecibo Observatory, HC 3, Box 53995, Arecibo, PR 00612*

csalter@naic.edu

Tapasi Ghosh

*NAIC, Arecibo Observatory, HC 3, Box 53995, Arecibo, PR 00612*

tghosh@naic.edu

## ABSTRACT

We present results from an on-going survey for the H I 21 cm line and the OH 18 cm lines in IR galaxies with the Arecibo 305 m Radio Telescope. The observations of 85 galaxies extracted from the 2 Jy IRAS-NVSS sample in the R.A. (B1950) range  $20^{\text{h}}-00^{\text{h}}$  are reported in this paper. We detected the H I 21 cm line in 82 of these galaxies, with 18 being new detections, and the OH 18 cm lines in 7 galaxies, with 4 being new detections. In some cases, the H I spectra show the classic double-horned or single-peaked emission profiles. However, the majority exhibit distorted H I spectral features indicating that the galaxies are in interacting and/or merging systems. From these H I and OH observations, various properties of the sample are derived and reported.

*Subject headings:* galaxies: general — galaxies: interactions — masers — radio emission lines — techniques: spectroscopic

## 1. Introduction

At bolometric luminosities above  $10^{11}L_{\odot}$ , infrared (IR) galaxies become the dominant population of extragalactic objects in the local universe ( $z \leq 0.3$ ). These galaxies are subdivided into three categories: luminous (LIRGs,  $L_{\text{IR}} > 10^{11}L_{\odot}$ ), ultraluminous (ULIRGs,  $L_{\text{IR}} > 10^{12}L_{\odot}$ ), and hyperluminous (HyLIRGs,  $L_{\text{IR}} > 10^{13}L_{\odot}$ ; Sanders & Mirabel 1996). Even though these IR galaxies are relatively rare, comprising less than 6% of the total IR energy density in the local Universe (Soifer & Neugebauer 1991), some studies suggest that the majority of galaxies with  $L_{\text{B}} > 10^{11}L_{\odot}$  go through a stage of intense IR emission (Soifer et al. 1987).

Most IR galaxies with  $L_{\text{IR}} < 10^{11}L_{\odot}$  are single, gas-rich spirals, and their IR emission can be accounted for by star formation. In the luminosity range  $10^{11} < L_{\text{IR}} < 10^{12}L_{\odot}$ , most of the galaxies are interacting/merging systems with enormous quantities of molecular gas ( $\sim 10^{10} M_{\odot}$ ). At the lower end of this range, the bulk of the IR luminosity is due to warm dust grains heated by a nuclear starburst, while active galactic nuclei (AGN) become increasingly important at higher luminosities. Galaxies with  $L_{\text{IR}} > 10^{12}L_{\odot}$  are believed to be advanced mergers powered by a combination of starburst and AGN (Sanders & Mirabel 1996).

Previous H I observations of IR galaxies have revealed very broad absorption lines in ULIRGs, indicating rotation plus large amounts of turbulent gas (Mirabel 1982). High angular resolution Very Large Array (VLA) and Very Long Baseline Interferometry (VLBI) observations show that these galaxies have the absorbing H I situated in the inner few hundred parsecs along the line of sight to the nuclear continuum sources (Baan et al. 1987; Momjian et al. 2003).

Several OH 18 cm absorption and megamaser (hereafter OHM) emission surveys of ULIRGs have also been published (Baan 1989; Darling & Giovanelli 2000, 2001, 2002). Baan (1989) concluded that the OHM emission usually occurs in galaxies with higher far-IR (FIR) luminosities and flatter 100–25  $\mu\text{m}$  spectra rather than in those with OH 18 cm absorption features.

Here, we report results from an on-going spectroscopic survey with the Arecibo Radio Telescope<sup>1</sup> targeting the H I 21 cm and the main and satellite OH 18 cm lines of 85 IR galaxies from the 2-Jy IRAS-NVSS sample (Yun, Reddy & Condon 2001). In this paper, we adopt  $H_0 = 71 \text{ km s}^{-1} \text{ Mpc}^{-1}$ ,  $\Omega_M = 0.27$ , and  $\Omega_{\Lambda} = 0.73$ .

---

<sup>1</sup>The Arecibo Observatory is part of the National Astronomy and Ionosphere Center, which is operated by Cornell University under a cooperative agreement with the National Science Foundation.

## 2. The Sample

The 85 galaxies reported in this paper are a first set of objects extracted from the 2-Jy IRAS-NVSS sample (Yun, Reddy & Condon 2001), which consists of 1809 IRAS sources that have  $S_{60\ \mu\text{m}} \geq 2$  Jy with 1.4 GHz radio counterparts from the NRAO-VLA Sky Survey (NVSS; Condon et al. 1998). The selection criteria for our full sample are: (1) they lie within the area of sky accessible to the Arecibo telescope (i.e.  $-1^\circ < \text{declination} < 38^\circ$ ), (2) have  $L_{\text{FIR}} \geq 7 \times 10^9 L_\odot$ , and (3) have heliocentric velocities between 0 and 50,000 km s<sup>-1</sup>. The number of galaxies that meet these criteria is 582. The present study includes 85 of these galaxies within the R.A. (B1950) range 20<sup>h</sup>–00<sup>h</sup>.

Table 1 presents the 85 galaxies reported in the paper. Column (1) gives the IRAS names of the galaxies, and column (2) lists other common designations, where applicable. Column (3) and (4) are the Right Ascensions and Declinations actually observed in J2000 coordinates. Column (5) lists the optical redshifts retrieved from the NASA/IPAC Extragalactic Database (NED). Column (6) is the 60  $\mu\text{m}$  flux densities from the IRAS Faint Source Catalog (FSC), where available. Galaxies marked with an asterisk do not have 60  $\mu\text{m}$  flux density measurements in the FSC, and for these the IRAS Point Source Catalog (PSC) values are given instead. Column (7) is the 1.4 GHz flux densities from the NVSS survey. Column (8) provides the morphologies listed in NED and in the Hyperleda database (Paturel et al. 2003).

## 3. Observations and Data Reduction

The 85 galaxies were observed with the 305 m Arecibo radio telescope between July and November 2004 using the L-band wide receiver. The low frequency cut-off of the receiver is 1100 MHz, well below the heliocentric velocity limit of 50,000 km s<sup>-1</sup> for our sample. The four independent boards of the Arecibo Interim Correlator were utilized to simultaneously observe the following redshifted transitions: the H I 21 cm line (1420.40575 MHz), both of the OH 18 cm main lines (1665.4018 and 1667.359 MHz), and the two OH 18 cm satellite lines at 1612.231 and 1720.530 MHz. A bandwidth of 12.5 MHz (dual polarization) was used for each correlator board with 1024 spectral channels per polarization. The three boards that targeted the H I and the OH satellite lines were centered at the frequencies of the respective redshifted transitions, while the central frequency of the board targeting the two OH 18 cm main lines was set to the redshifted value of the 1667.359 MHz transition. We used the total-power, position-switching (ON-OFF), observational mode for all the objects in our sample. However, the spectra of some sources showed significant baseline ripples. For these sources, the Double Position Switching (DPS; Ghosh & Salter 2002) observing technique,

which requires observing a nearby bandpass calibrator, was utilized in order to minimize the baseline ripples in their spectra.

The data were reduced using the standard Arecibo Observatory (AO) IDL routines and special-purpose codes developed by AO staff. The spectra of the sources observed with the ON-OFF mode were converted to units of flux density using the noise-diode calibration and the standard gain curves. For sources observed in DPS mode, the flux densities of the bandpass calibrators were used to convert the ratio spectra to Janskys. Hanning smoothing was applied to the raw spectra, and after averaging the two polarizations, a 9-channel boxcar smoothing was applied to further improve the signal-to-noise ratio. The resulting spectral resolution was 112 kHz. Polynomial baselines were fitted to the resulting spectra and subtracted from them to produce the final spectra used to derive the velocity, velocity widths, the integrated intensities of the lines, and the rms noises on the spectra for each object.

## 4. Results

### 4.1. H I 21 cm Line Spectra

We detected 21 cm H I in emission and/or absorption in 82 of the 85 galaxies; 18 of these had not been previously reported in the literature. There were 7 sources with both absorption and emission features in their spectra, and 3 with pure absorption. IRAS 21396+3623, one of the three non-detections, was observed at an erroneous frequency because its redshift was incorrectly listed in the 2-Jy IRAS NVSS Sample. This source has not been included in the analysis of the data.

Figure 1 shows the spectra of the 18 new H I 21 cm detections, while Figure 2 shows our spectra for those sources with previously published H I 21 cm detections. We note that Figures 1 and 2 present the spectra before subtraction of the fitted polynomials. These hence demonstrate the quality of the raw baselines, and reveal any continuum emission associated with the source.

Some of the 21 cm H I emission spectra in our sample show single peak or double horn profiles, both characteristic of non-interacting galaxies. However, the majority of the galaxies observed have distorted spectra as expected for interacting/merging systems. The galaxies in such systems have higher IR luminosities than do non-interacting spirals.

Table 2 summarizes the physical properties derived from the H I emission spectra of the galaxies in our sample, including non-detections (marked by an asterisk). The values in this table are derived using the baseline-subtracted spectra. Sources marked by  $\diamond$  are those

observed in DPS mode. Seven sources (indicated by † in Table 2) exhibit both emission and absorption features in their spectra. For these, the table contains information from the emission part of the spectra, and the derived flux density integrals and neutral hydrogen masses should be considered to be lower limits because some of the emission might be masked by the absorption features. The absorption components are presented separately later in this section. Column (1) in Table 2 lists the IRAS names of the galaxies. Column (2) gives the total on-source integration times. Column (3) lists the rms noise levels. Column (4) lists the heliocentric velocities at which the H I emission lines are centered. For non-detections, the values correspond to the optical velocities retrieved from NED. Column (5) is the full velocity widths at half maximum (FWHM) for the observed emission lines. Column (6) is the flux density integrals ( $\int S dv$ ) of the H I lines. For non-detections, the values are  $3\sigma$  upper limits derived assuming  $\Delta V_{50} = 400 \text{ km s}^{-1}$ . Column (7) lists the luminosity distances ( $D_L$ ) of the galaxies derived using their respective velocities (column 4). Column (8) gives the logarithms of the FIR luminosities calculated using the equation (e.g. Sanders & Mirabel 1996):

$$L_{\text{FIR}}(L_{\odot}) = 3.96 \times 10^5 D_L^2 (2.58f_{60} + f_{100}) \quad (1)$$

where  $D_L$  is in Mpc, and  $f_{60}$  and  $f_{100}$  are respectively the 60 and 100  $\mu\text{m}$  flux densities in Jy. Column (9) is the logarithms of the total IR luminosities derived using the equation (e.g. Sanders & Mirabel 1996):

$$L_{\text{IR}}(L_{\odot}) = 5.67 \times 10^5 D_L^2 (13.48f_{12} + 5.16f_{25} + 2.58f_{60} + f_{100}). \quad (2)$$

Column (10) lists the logarithms of the total neutral hydrogen mass values derived using the expression (Roberts 1975) :

$$M_{\text{HI}}(M_{\odot}) = 2.36 \times 10^5 D_L^2 \int S dv \quad (3)$$

where the  $\int S dv$  is the flux density integral in  $\text{Jy km s}^{-1}$ .

Table 3 lists the parameters of the H I absorbers. The properties of the H I absorption lines are derived from spectra where the flux densities were scaled into optical depths ( $\tau$ ) and plotted against heliocentric velocity. The values in this table are also obtained using the baseline-subtracted spectra. Column (1) lists the IRAS names of the galaxies. Column (2) lists their luminosity distances. These distances are derived using the velocity of the H I emission line for sources that exhibit both H I emission and absorption (from Table 2), and the optical redshift values (from Table 1) for sources that exhibit H I absorption only. Columns (3) and (4) give the logarithms of the FIR and the total IR luminosities calculated using equations 1 and 2, respectively. Column (5) is the total on-source integration times. Column (6) lists the rms noise levels. Column (7) lists the heliocentric velocities at the peak

of the absorption feature in each source. Column (8) is the FWHM velocity values of the overall observed absorption profile. Column (9) lists the peak optical depths. Column (10) gives the H I column densities divided by the spin temperature which are derived assuming a covering factor of unity and using the equation (e.g. Rohlfs 1986):

$$N(\text{HI})/T_s \text{ (cm}^{-2} \text{ K}^{-1}\text{)} = 1.823 \times 10^{18} \int \tau dv. \quad (4)$$

## 4.2. OH 18 cm Line Spectra

We detected OH 18 cm main lines in 7 galaxies; 3 in emission (OHMs) and 4 in absorption. Of these, 1 OHM and 3 OH absorbers are new detections (Figure 3). For these spectra, the 1667.359 MHz line was used for deriving the velocity scale. There were no detections of the OH 18 cm satellite lines at 1612 and 1720 MHz in any of the galaxies of our sample. Figure 4 shows the spectra of the 3 sources with previously known OH 18 cm main lines. As for the H I 21 cm spectra in Figures 1 & 2, Figures 3 & 4 present the final spectra, but without the subtraction of fitted polynomials.

Table 4 summarizes the parameters derived from the OHM detections. The values in this table are derived using the baseline-subtracted spectra. Column (1) lists the IRAS names of the galaxies. Column (2) is the total on-source integration times. Column (3) gives the rms noise levels, and column (4) lists the heliocentric velocities at the center of the 1667.359 MHz line emission. Columns (5) and (8) are the peak flux densities of the 1667 and 1665 MHz lines respectively, columns (6) and (9) are their full velocity widths at half maximum, and columns (7) and (10) list their integrated flux densities. Column (11) lists the hyperfine ratios obtained by dividing the integrated flux density of the 1667 MHz line by that at 1665 MHz for each source. In thermodynamic equilibrium conditions, this ratio would be  $R_H = 1.8$ , and it increases as the saturation of a masing region increases. Column (12) lists the logarithms of the predicted OH luminosities (in units of  $L_\odot$ ) which have been calculated using the following equation from Kandalian (1996):

$$\log L_{\text{OH}}^{\text{pred}} = 1.38 \log L_{\text{FIR}} - 14.02, \quad (5)$$

while column (13) gives the logarithms of the measured isotropic OH line luminosities, which represents the combined integrated flux densities of the two OH 18 cm main lines. Columns (14) and (15) are the rms noise values for the 1612 and 1720 MHz transitions. Blank fields in these two columns indicate that the rms noise values could not be estimated because of severe radio frequency interference (RFI).

Table 5 lists the parameters derived from the OH absorption lines. The values in this

table are derived using the baseline-subtracted spectra. Column (1) is the IRAS names of the galaxies. Column (2) is the total on-source integration times. Column (3) gives the rms noise levels, and column (4) lists the heliocentric velocities at the center of the 1667.359 MHz absorption lines. Columns (5) and (9) are the full velocity widths at half maximum of the 1667 and 1665 MHz lines respectively, columns (6) and (10) are their peak optical depths, and columns (7) and (11) are their integrated optical depths. Column (8) is the column densities of the 1667 MHz lines divided by the excitation temperature using the following equation from Turner (1973) and assuming a covering factor of unity:

$$N_{\text{OH}}/T_{\text{ex}}(\text{cm}^{-2} \text{ K}^{-1}) = 2.35 \times 10^{14} \int \tau dv \quad (6)$$

where  $\int \tau dv$  is the integrated optical depth of the 1667 MHz absorption feature given in column (7). Column (12) lists the hyperfine ratios, obtained by dividing the integrated optical depths of the two main lines. Columns (13) and (14) are the rms noise values for the 1612 and 1720 MHz transitions. Blank fields in these two columns indicate that the rms noise values could not be estimated because of severe RFI.

Table 6 lists relevant data for all sources with no detections in the OH 18 cm mainlines. Column (1) is the IRAS names of the galaxies. Column (2) lists the rms noise values of the OH 18 cm main line non-detections. Column (3) is the logarithms of predicted OH luminosities from equation 5, and column (4) is the logarithms of the maximum OH luminosities for the 1667 MHz main line determined using the equation (from Darling & Giovanelli 2000):

$$L_{\text{OH}}^{\text{max}} = 4\pi D_L^2 1.5\sigma \frac{\Delta V}{c} \frac{\nu_o}{(1+z)} \quad (7)$$

where  $D_L$  is the luminosity distance,  $\sigma$  is the rms noise value listed in column (2),  $\Delta V = 150 \text{ km s}^{-1}$ ,  $c$  is the speed of light,  $\nu_o$  is the rest frequency of the 1667 MHz transition, and  $z$  is the redshift. Columns (5) and (6) are the rms noise values of the 1612 and 1720 MHz transitions. Blank fields in this table indicate that the rms noise values could not be estimated because of severe RFI.

## 5. Analysis and Discussion

Here we report preliminary statistical analysis for the observed sample. More detailed analysis and conclusions will be presented after completion of the full survey with all 582 galaxies.

Figure 5 (*top*) shows the well established radio–FIR correlation through a logarithmic plot of the 1.4 GHz continuum luminosities versus the FIR luminosities for the galaxies in

our sample. The derived correlation coefficient is 88%. Figure 5 (*bottom*) shows a logarithmic plot of the 1.4 GHz continuum luminosities versus the total IR luminosities. The correlation coefficient here is 89%.

This remarkably tight linear correlation between the total radio continuum emission and the IR (or FIR) luminosities is well known for “normal” galaxies where the main energy source is not due to a supermassive black hole (Condon 1992). The most obvious interpretation of this correlation is the presence of massive stars that provide both relativistic particles via subsequent supernova events, and heat the interstellar dust which radiates at IR (or FIR) wavelengths (Helou, Soifer & Rowan-Robinson 1985; Wunderlich & Klein 1988; Condon 1992).

Figure 6 shows logarithmic plots of the H I mass versus the FIR (*top*) and IR (*bottom*) luminosities for the observed sample. Both plots show extremely weak correlations with coefficients of 42% in each. Figure 7 shows a logarithmic plot of the H I mass versus the 1.4 GHz radio luminosity. The correlation coefficient here is 53%. These plots suggest that the total neutral gas content and star formation activity traced through the radio luminosities or the IR luminosities are only weakly correlated for this sample. This is consistent with the scenario that atomic gas has first to be converted into molecular gas to form stars, and that the molecular gas content itself correlates well with star formation (Wong & Blitz 2002). In Table 7, we present the mean and median H I mass values of galaxies with H I 21 cm emission as a function of total-IR luminosity bins. The numbers reflect a general trend of higher H I mass values at higher IR luminosities, consistent with the weak correlation seen in Figure 6-*bottom*. We utilize the values presented in this table in our notes on individual objects in §6.

In our observed sample, several galaxies show either H I absorption or both H I emission and absorption. Binning the sample in  $L_{\text{IR}}$  (Table 8a) reveals that sources with higher IR luminosities have the greater likelihood of showing H I absorption. For instance, 38.5% of the sources with  $L_{\text{IR}} \geq 10^{11.50} L_{\odot}$  show H I absorption, while only 10.3% of sources with  $10^{11.00} L_{\odot} \leq L_{\text{IR}} \leq 10^{11.49} L_{\odot}$ , and 6.3% of sources with  $10^{10.50} L_{\odot} \leq L_{\text{IR}} \leq 10^{10.99} L_{\odot}$  show H I absorption. No H I absorption is seen in sources with  $L_{\text{IR}} \leq 10^{10.49} L_{\odot}$  (see Table 8a). Thus, while we cannot say anything about traditionally defined ULIRGs ( $L_{\text{IR}} \geq 10^{12} L_{\odot}$ ) because of their rarity in our observed sample, it appears that galaxies with  $L_{\text{IR}} \geq 10^{11.50} L_{\odot}$  have a greater likelihood of showing H I absorption. We now explore whether this trend could arise due to a selection effect.

While the flux density of H I emission is proportional to  $L_{\text{HI}}/D^2$ , where  $D$  is the distance to the galaxy, the flux density dip of an absorption corresponding to a given optical depth is proportional to the background continuum flux density that is being absorbed. In Table 8b



we present the calculated mean and median NVSS flux densities for the galaxies in our observed sample as a function of  $L_{\text{IR}}$  bins, to investigate whether galaxies having  $L_{\text{IR}} \geq 10^{11.50} L_{\odot}$  preferentially have higher flux densities. Table 8b shows that the radio flux densities in our sample do not correlate with IR luminosity. However, we do find for those galaxies showing H I absorption in the two highest luminosity bins, that the mean flux densities are about double the mean values for all galaxies in those bins. As a second possible effect, the  $L_{\text{IR}} \geq 10^{11.50} L_{\odot}$  absorbers might have a higher covering factor than those of lower luminosity e.g., their continuum emission may mostly be in a compact nucleus vs. more extended continuum emission for the others, with the absorption arising principally in the nuclear regions. However, whether this is the case or not, we do find a difference in the incidence of H I absorption between IR galaxies with  $L_{\text{IR}} \geq 10^{11.50} L_{\odot}$  and those with lower IR luminosities, i.e., the galaxies with higher IR luminosities have higher H I column densities on the lines of sight to the continuum sources, and/or their continuum emission is confined to more compact regions.

In Table 9, we present the statistics of OH detections (absorption or emission) as a function of  $L_{\text{IR}}$  bins. The total number of sources per  $L_{\text{IR}}$  bin in this table excludes galaxies with OH main line spectra severely affected by RFI. Here we note that all 3 of the OH emitters have  $L_{\text{IR}} \geq 10^{11.50} L_{\odot}$ , while the two detections for  $10^{10.50} L_{\odot} \leq L_{\text{IR}} \leq 10^{10.99} L_{\odot}$  are both absorbers. However, despite the small numbers in this subgroup, it is strongly suggestive that OH-detected sources (emitters and absorbers) are found primarily in galaxies with  $L_{\text{IR}} \geq 10^{11.50} L_{\odot}$ .

## 6. Notes on Individual Objects

**IRAS 20210+1121:** This galaxy is at a redshift of  $z = 0.0564$ , and is one of two sources with no H I detection in our observed sample, with the other source being IRAS 23410+0228 ( $z = 0.0912$ ; see below). Its IR luminosity is  $10^{11.90 \pm 0.09} L_{\odot}$  and the derived  $3\sigma$  upper limit for its H I mass, assuming a  $400 \text{ km s}^{-1}$  velocity width, is  $10^{9.86} M_{\odot}$ . In the sample presented in this paper, sources with  $L_{\text{IR}} > 10^{11.50} L_{\odot}$  and detected H I emission have a H I median mass value of  $10^{9.86} M_{\odot}$  and a mean value of  $10^{9.99 \pm 0.10} M_{\odot}$ . This suggests that IRAS 20210+1121 is likely to be hydrogen deficient. However, at IR luminosities  $> 10^{11.50} L_{\odot}$ , there are four sources in our sample with H I detections that have H I masses  $< 10^{9.86} M_{\odot}$ . Therefore, observations with longer integration time are needed to establish whether IRAS 20210+1121 is truly hydrogen deficient.

**IRAS 20332+0805:** Our estimated heliocentric velocity for this galaxy of  $7967.3 \pm 8.9 \text{ km s}^{-1}$  differs from the single optically-measured value of  $8353 \pm 57 \text{ km s}^{-1}$  at the  $6.8 \sigma$

level. While the velocity of the peak H I emission is somewhat higher than the measured central velocity, the discrepancy is still significant.

**IRAS 21054+2314:** This galaxy, with a redshift of  $z = 0.0487$ , shows both H I 21 cm emission and absorption, and OH 1667 MHz absorption (Figures 1 and 3). These detections have not been previously reported in the literature. Its H I absorption feature is at a higher velocity than the emission, suggesting infalling gas towards the central continuum source.

**IRAS 21442+0007:** This source shows a previously unreported H I 21 cm absorption line at  $cz = 22241 \text{ km s}^{-1}$  or  $z = 0.0742$ . However, its H I spectrum (Figure 1) also shows a wide, previously unknown, emission line centered at  $cz = 22555 \text{ km s}^{-1}$  or  $z = 0.0752$  with  $\Delta V_{50\%} = 207.3 \text{ km s}^{-1}$ . This emission does not seem to be arising from the target source IRAS 21442+0007, but from the nearby galaxy SDSS J214651.97+002302.2 at  $cz = 22575 \pm 49 \text{ km s}^{-1}$  (or  $z = 0.0753 \pm 0.0002$ ). The projected angular separation between the two sources is 1.8 arcmin, meaning that SDSS J214651.97+002302.2 was situated close to the half-power point of the  $\sim 3.5$  arcmin L-band beam in our observations. After correcting for the beam, we derive an H I mass value of  $9 \times 10^9 M_{\odot}$  for SDSS J214651.97+002302.2. The proximity of IRAS 21442+0007 and SDSS J214651.97+002302.2 in both angular distance and velocity suggests that they may be members of the same galaxy cluster or group.

**IRAS 22045+0959:** Also known as NGC 7212, this triple system has a cataloged redshift of  $z = 0.0266$ . Optical studies show it to be a system of three interacting galaxies lying within an area of radius  $\approx 0.5$  arcmin. NGC 7212 NED 1 is a small spiral of undetermined redshift. NED 7212 NED 2 has an optical spectrum characteristic of a Seyfert 2 nucleus, though showing a Seyfert 1-like spectrum in polarized light (e.g., Vorontsov-Velyaminov & Arhipova 1963; Wasilewski 1981). Its optical radial velocity is given as  $7927 \pm 18 \text{ km s}^{-1}$  by Falco et al. (1999), but as  $7800 \text{ km s}^{-1}$  (with no formal error) by Strauss et al. (1992). NED 7212 NED 3 appears to be interacting strongly with NED 2, and has an optical radial velocity of  $8167 \pm 74 \text{ km s}^{-1}$  (Falco et al. 1999).

The IR luminosity of the system is  $L_{\text{IR}} = 10^{11.15 \pm 0.10} L_{\odot}$ . Our calculated H I mass for the system is  $10^{10.01 \pm 0.02} M_{\odot}$ , slightly higher than the median ( $10^{9.78} M_{\odot}$ ) and the mean ( $10^{9.69 \pm 0.08} M_{\odot}$ ) we find for sources with IR luminosities in the range  $10^{11} - 10^{11.49} L_{\odot}$ . Our H I spectrum (Figure 2) may represent two spiral-galaxy-like, double-horned spectra. The radial velocity of NED 3 agrees well with the higher redshift feature. However, while the Strauss et al. (1992) velocity for NED 2 would be compatible with the lower redshift feature, the Falco et al. (1999) velocity would place the systemic velocity near the “central gap” between the two features. The depth of this gap between the two features drops to slightly more than  $3\sigma$  below the continuum level. Hence it could represent H I absorption, while also being compatible with a lack of H I emission at that velocity. Clearly, high resolution H I

synthesis mapping is needed to resolve the actual situation in this system. Here, we have taken the H I classification of IRAS 22045+0959 to be a mixture of emission and absorption (see Table 3), though we caution that this may need revision following future observations.

**IRAS 22523+3156:** This object also displays previously unreported H I and OH lines (Figures 1 and 3). IRAS 22523+3156 has a relatively low IR luminosity, and is at a redshift of  $z = 0.0212$ . Its H I spectral shape is peculiar, with a deep absorption feature in the middle of the emission line. Its OH spectrum displays two nicely defined absorption features of the redshifted 1667 and 1665 MHz main lines. The H I and OH absorption lines arise at the same velocity (see Tables 3 & 5), indicating that they originate from the same region.

The ratio of  $\int \tau dv$  for the 1667 and 1665 MHz absorption lines is  $1.88 \pm 0.03$ , comparable with the expected ratio in thermal equilibrium of 1.8. In thermal equilibrium, the satellite lines should be found with a hyperfine ratio relative to the 1667 MHz line of 0.111. The measured rms level for the 1720 MHz satellite line (Table 5) gives a  $3\sigma$  upper limit for this ratio of 0.131, indicating that our non-detection is not inconsistent with thermal equilibrium. This is especially the case as very low level RFI appears to be present near this satellite line in some of the data. No rms value was estimated for the 1612 MHz satellite line, because the spectrum was severely affected by RFI.

**IRAS 22595+1541:** Our H I spectrum for this target provides an estimated heliocentric velocity of  $2089.6 \pm 0.5 \text{ km s}^{-1}$ , differing at the  $7\sigma$  level from the weighted optically-measured value for the galaxy NGC 7465 (type SB0) of  $1977 \pm 16 \text{ km s}^{-1}$ . This galaxy is a member of the galaxy group RSCG 83 for which NED provides a H I velocity of  $2091 \pm 5 \text{ km s}^{-1}$  from the HIPASS H I survey. Within our 3.5 arcmin HPBW we could potentially be seeing emission from three galaxies, (a) NGC 7465; the prime target, (b) NGC 7464, an E1 pec galaxy with an optical radial velocity of  $1787 \pm 17 \text{ km s}^{-1}$ , and (c) NGC 7463, an SABb pec galaxy with an optical radial velocity of  $2439 \pm 24 \text{ km s}^{-1}$ . The very broad H I spectrum seen in Figure 2 suggests that in all probability we are seeing emission from all three, with that of NGC 7465 dominating.

**IRAS 23050+0359:** This galaxy, at  $z = 0.0474$ , is a new H I emission detection, but has a previously known OH megamaser which we also detect (Figures 1 and 4). It has a total IR luminosity of  $L_{\text{IR}} = 10^{11.67 \pm 0.16} L_{\odot}$ , making it one of the more IR luminous objects in our sample. The calculated H I mass from its distorted spectrum is  $10^{9.71 \pm 0.08} M_{\odot}$ ; a value that is slightly lower than the median ( $10^{9.86} M_{\odot}$ ) and the mean ( $10^{9.99 \pm 0.10} M_{\odot}$ ) for objects with IR luminosities greater than  $10^{11.50} L_{\odot}$  (Table 7).

**IRAS 23204+0601:** Also known as III Zw 103, this galaxy is at a redshift of  $z = 0.0560$ , and is also a new H I emission detection (Figure 1). With a total IR luminosity of

$L_{\text{IR}} = 10^{11.88 \pm 0.16} L_{\odot}$ , it is also one of the more IR luminous sources in our sample. We were unable to determine if there is OH emission/absorption in this source, because the spectra of all its main and satellite lines were severely affected by RFI. Its H I mass ( $10^{9.76 \pm 0.07} M_{\odot}$ ) is lower than the median and mean of galaxies with comparable IR luminosities (Table 7).

**IRAS 23327+2913:** Both the H I and OHM emission lines (Figures 1 and 3) of this ULIRG ( $z = 0.1067$ ) are new detections. A study by Dinh-V-Trung et al. (2001) showed that this object is a system of two interacting galaxies separated by 20 kpc. Its northern component is disturbed, while the southern component is a normal spiral with a very thick bar structure. High resolution radio interferometric observations are needed to establish from which galaxy in this system the H I and OHM emission lines originate.

**IRAS 23410+0228:** This galaxy is at a redshift of  $z = 0.0912$ , which is the second highest redshift in our observed sample. It is one of two sources with no H I detection, with the other source being IRAS 20210+1121 ( $z = 0.0564$ ; see above). Its IR luminosity is  $10^{12.08 \pm 0.17} L_{\odot}$  and the derived  $3\sigma$  upper limit for its H I mass, assuming a  $400 \text{ km s}^{-1}$  velocity width, is  $10^{10.30} M_{\odot}$ . This H I mass limit is greater than the median and the mean H I mass values for sources with  $L_{\text{IR}} > 10^{11.50} L_{\odot}$ , which are  $10^{9.86} M_{\odot}$  and  $10^{9.99 \pm 0.10} M_{\odot}$ , respectively. Therefore, the non-detection of H I emission from this source does not necessarily imply hydrogen deficiency.

**IRAS 23532+2513:** This target consists of three galaxies lying within our HPBW at similar redshifts. These are, (a) a starburst galaxy (type spiral:HII) lying 14 arcsec from our pointing position with an optical radial velocity of  $17584 \pm 69 \text{ km s}^{-1}$ , (b) a peculiar Sy1 galaxy also 14 arcsec from our pointing with an optical radial velocity of  $17121 \pm 18 \text{ km s}^{-1}$ , and (c) a spiral:HII galaxy about 1 arcmin from our pointing with an optical radial velocity of  $17273 \pm 68 \text{ km s}^{-1}$ . Our broad H I spectrum (Figure 2) shows emission over the full range of velocities covered by the 3 component galaxies.

## 7. Acknowledgements

We thank the anonymous referee for valuable comments and suggestions. This research has made use of the NASA/IPAC Extragalactic Database (NED) which is operated by the Jet Propulsion Laboratory, California Institute of Technology, under contract with the National Aeronautics and Space Administration. We also acknowledge the usage of the HyperLeda database (<http://leda.univ-lyon1.fr>). M.X.F. is grateful for support from NAIC-Arecibo Observatory during a summer research assistantship.

## REFERENCES

- Baan, W. A., van Gorkom, J. H., Schmelz, J. T., Mirabel, I. F. 1987, *ApJ*, 313, 102
- Baan, W. A. 1989, *ApJ*, 338, 804
- Condon, J. J. 1992, *ARA&A*, 30, 575
- Condon, J. J., Cotton, W. D., Greisen, E. W., Yin, Q. F., Perley, R. A., Taylor, G. B., Broderick, J. J. 1998, *AJ*, 115, 1693
- Darling, J., & Giovanelli, R. 2000, *AJ*, 119, 3003
- Darling, J., & Giovanelli, R. 2001, *AJ*, 121, 1278
- Darling, J., & Giovanelli, R. 2002, *AJ*, 124, 100
- Dinh-V-Trung, Lo, K. Y., Kim, D.-C., Gao, Yu, Gruendl, R. A. 2001, *ApJ*, 556, 141
- Falco, E. E., Kurtz, M. J., Geller, M. J., et al. 1999, *PASP*, 111, 438
- Ghosh, T., & Salter, C.J. 2002, in *ASP Conf. Ser. 278, Single-Dish Radio Astronomy: Techniques and Applications*, ed. S. Stanimirovic, D. Altschuler, P. Goldsmith, & C. Salter, (San Francisco: ASP), 521
- Helou, G., Soifer, B. T., & Rowan-Robinson, M. 1985, *ApJ*, 298, L7
- Kandalian, R. A. 1996, *Astrophysics*, 39, 237
- Mirabel, I. F. 1982, *ApJ*, 260, 75
- Momjian, E., Romney, J. D., Carilli, C. L., Troland, T. H., 2003, *ApJ*, 597, 809
- Paturel, G., Petit, C., Prugniel, Ph., Theureau, G., Rousseau, J., Brouty, M., Dubois, P., Cambresy, L. 2003, *A&A*, 412, 45
- Roberts, M. S. 1975, in *Galaxies and the Universe*, ed. A. Sandage, M. Sandage, & J. Kristian (Chicago : Univ. Chicago Press), 309
- Rohlfs, K., 1986, *Tools of Radio Astronomy*, (Springer-Verlag)
- Sanders, D. B., & Mirabel, I. F. 1996, *ARA&A*, 34, 749
- Soifer, B. T., & Neugebauer, G. 1991, *AJ*, 101, 354

- Soifer, B. T., Sanders, D. B., Madore, B. F., Neugebauer, G., Danielson, G. E., Elias, J. H., Lonsdale, Carol J., Rice, W. L. 1987, *ApJ*, 320, 238
- Strauss, M. A., Huchra, J. P., Davis, M., Yahil, A., Fisher, K. B., Tonry, J. L. 1992, *ApJS*, 83, 29
- Turner, B. E. 1973, *ApJ*, 186, 357
- Vorontsov-Velyaminov, B. A., & Arkhipova, V. P. 1963, *Morphological Catalogue of Galaxies, Part III (Trudy Astr. Inst. Sternberg 33)*, 68
- Wasilewski, A. J. 1981, *PASP*, 93, 560
- Wong, T., & Blitz, L. 2002, *ApJ*, 569, 157
- Wunderlich, E., & Klein, U. 1988, *A&A*, 206, 47
- Yun, M. S., Reddy, N. A., & Condon, J. J. 2001, *ApJ*, 554, 803

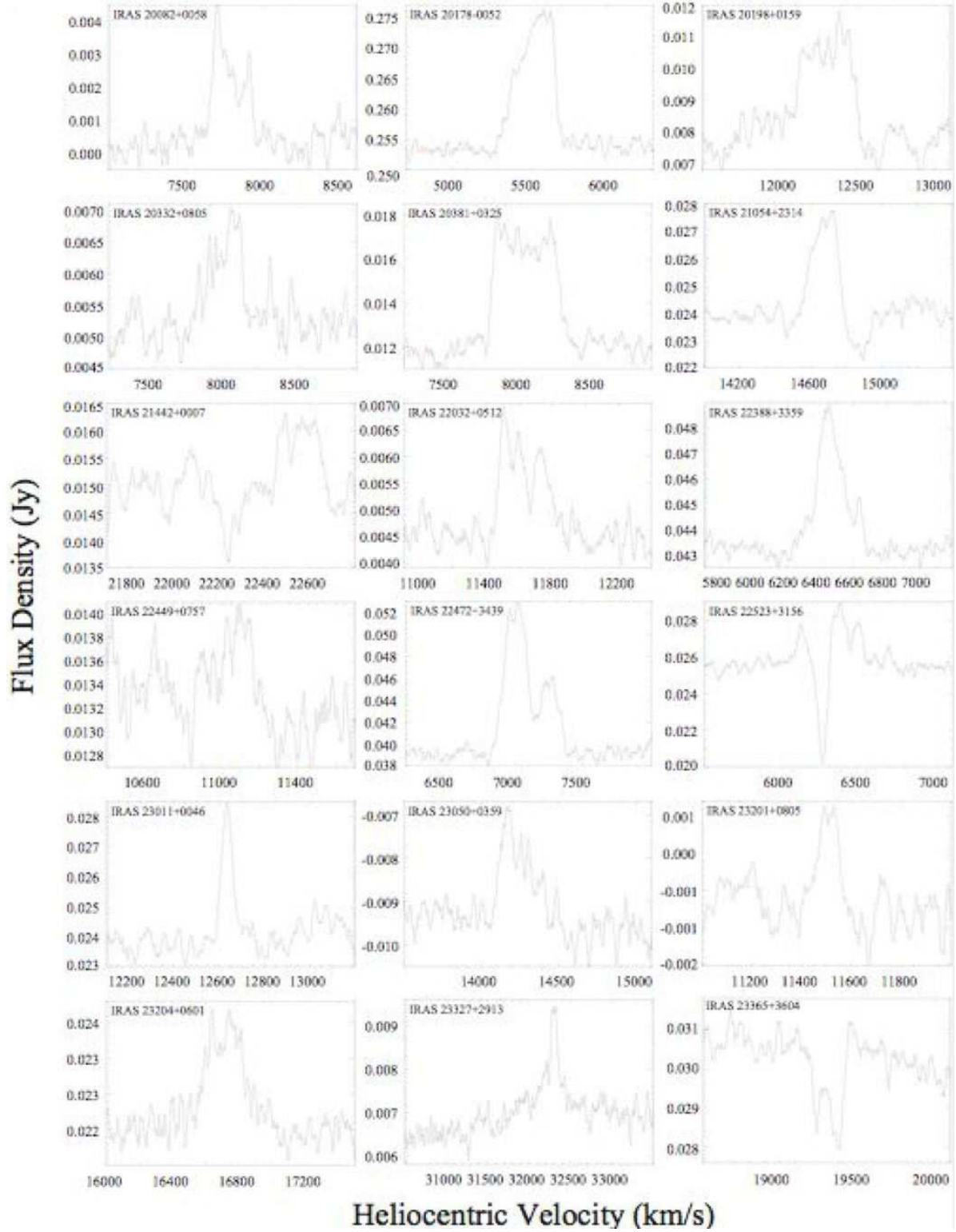


Fig. 1.— Spectra of the new H I 21 cm detections in our observed sample.

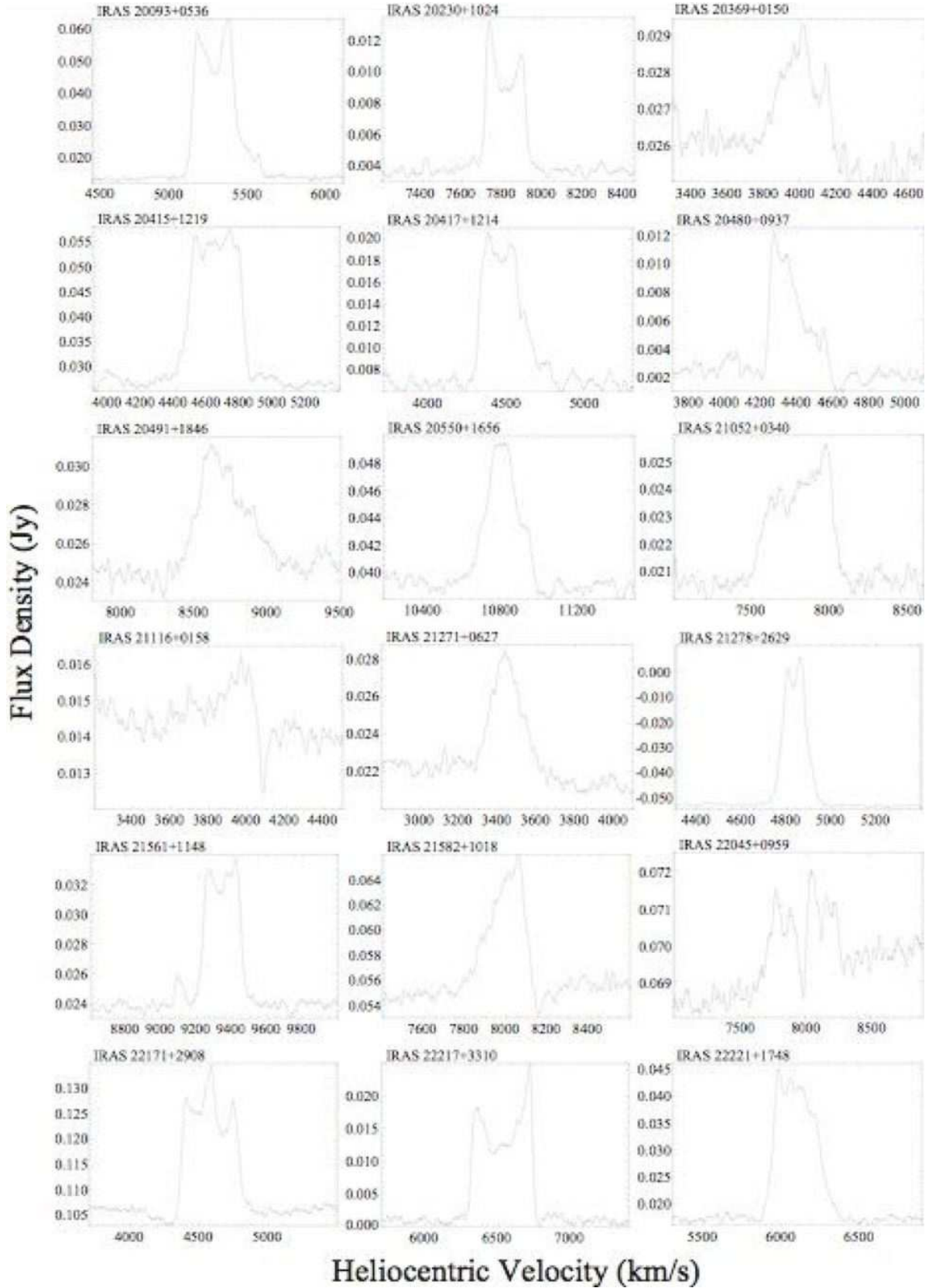


Fig. 2.— Spectra of the previously known H I 21 cm detections in our observed sample.



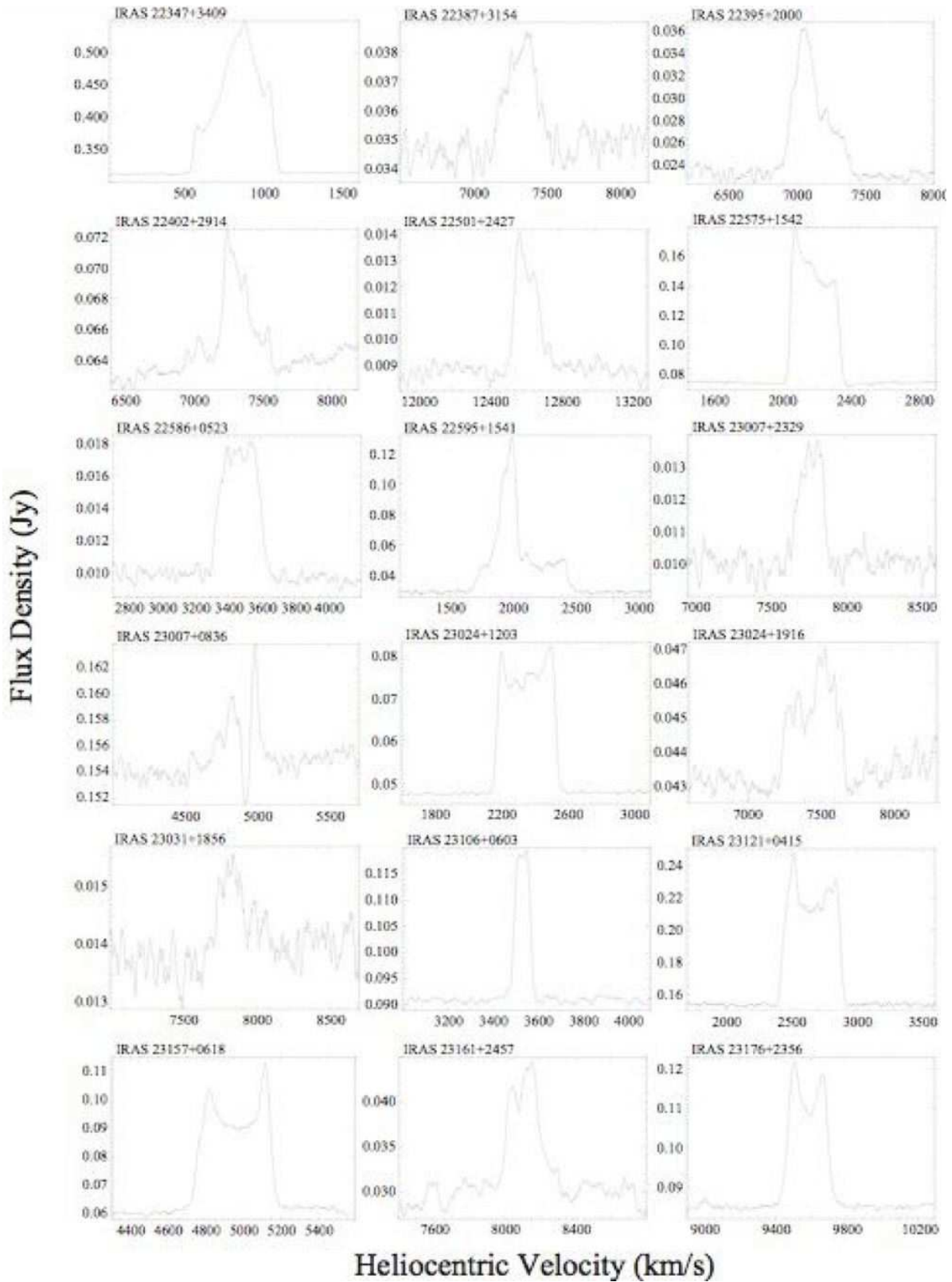


Fig. 2 cont.—

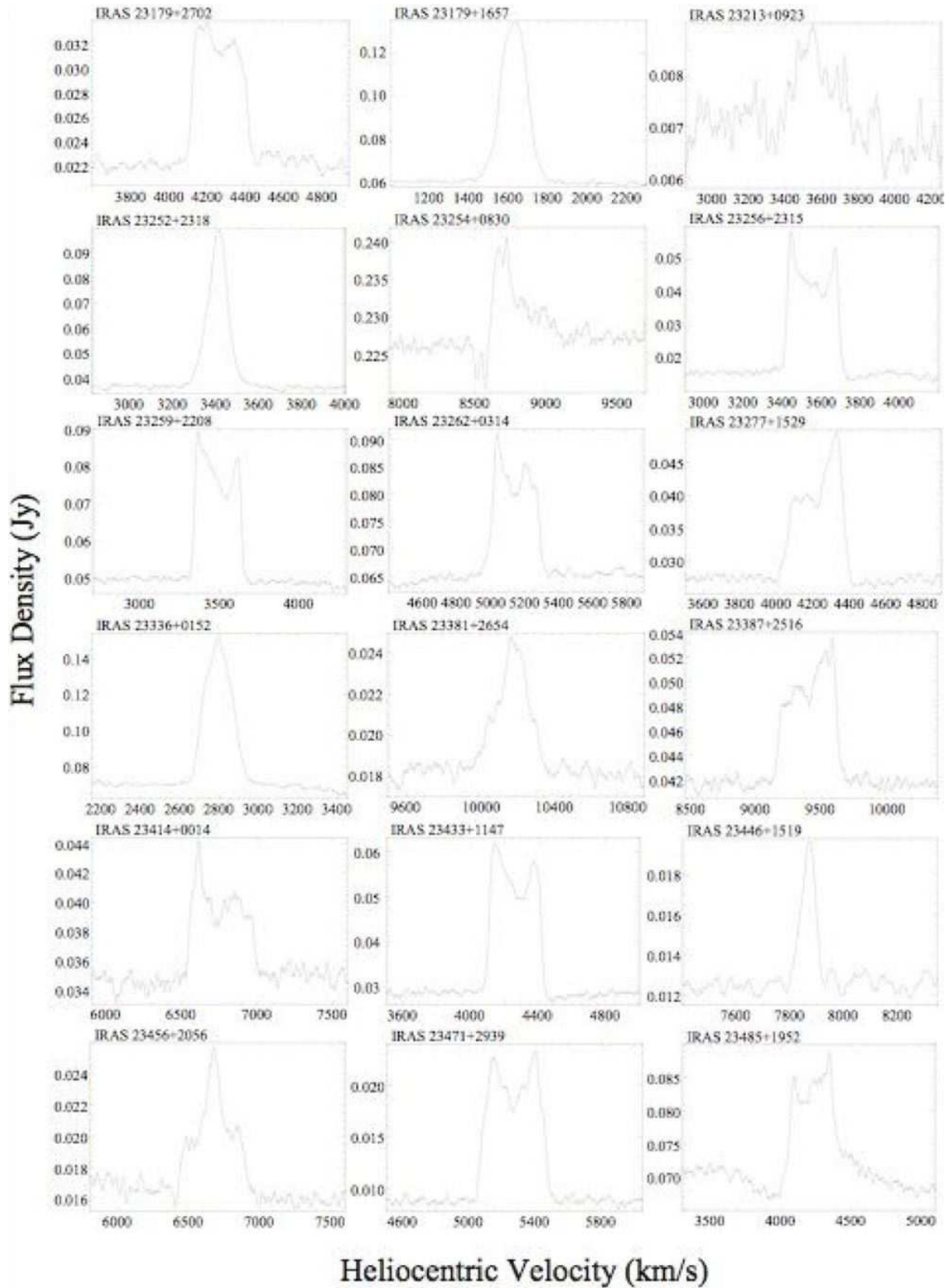


Fig. 2 cont.—

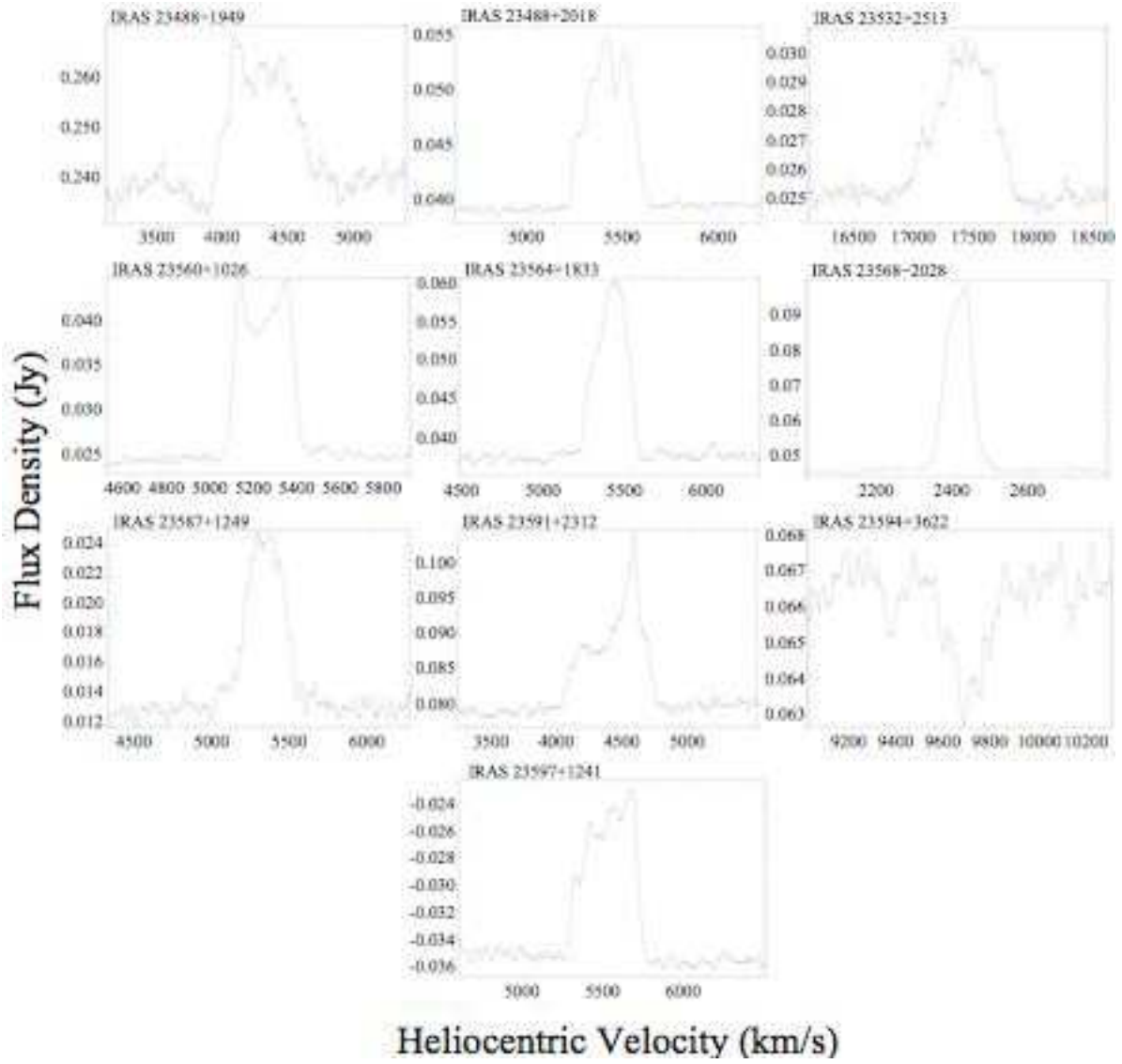


Fig. 2 cont.—

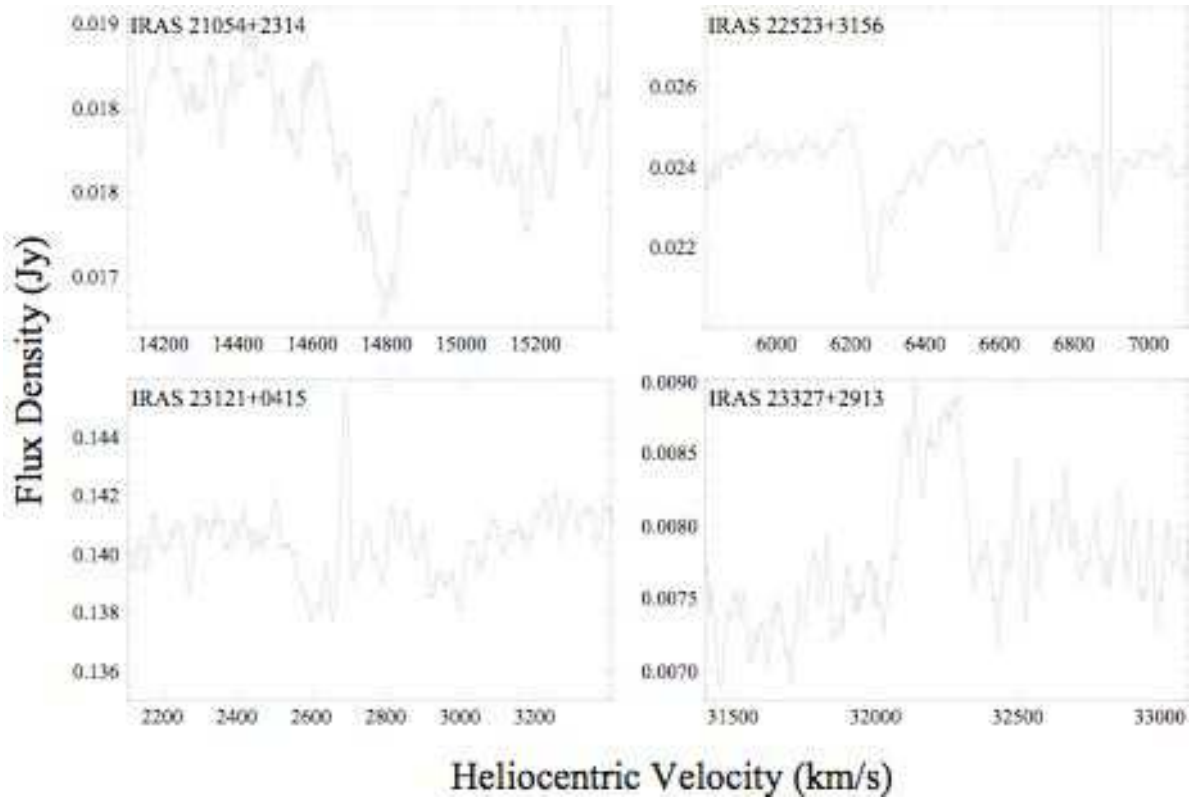


Fig. 3.— Spectra of the new OH 18 cm main line detections; three are in absorption, one in emission. The spectral features at  $6880 \text{ km s}^{-1}$  in the spectrum of IRAS 22523+3156 and at  $2685 \text{ km s}^{-1}$  in the spectrum of IRAS 23121+0415 are due to RFI. The spectra used the rest frequency of the 1667.359 MHz line for the velocity scale.

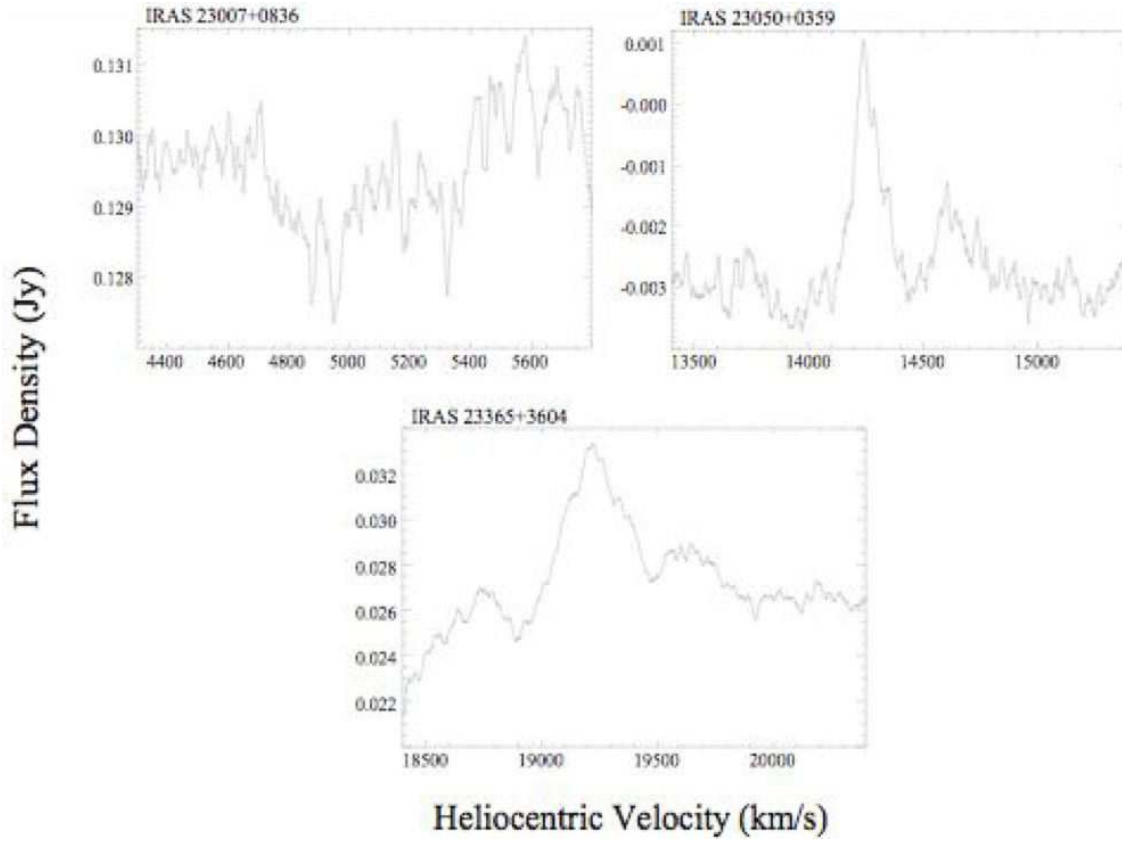


Fig. 4.— Spectra of the previously known OH 18 cm main line detections in our observed sample. The spectra used the rest frequency of the 1667.359 MHz line for the velocity scale.

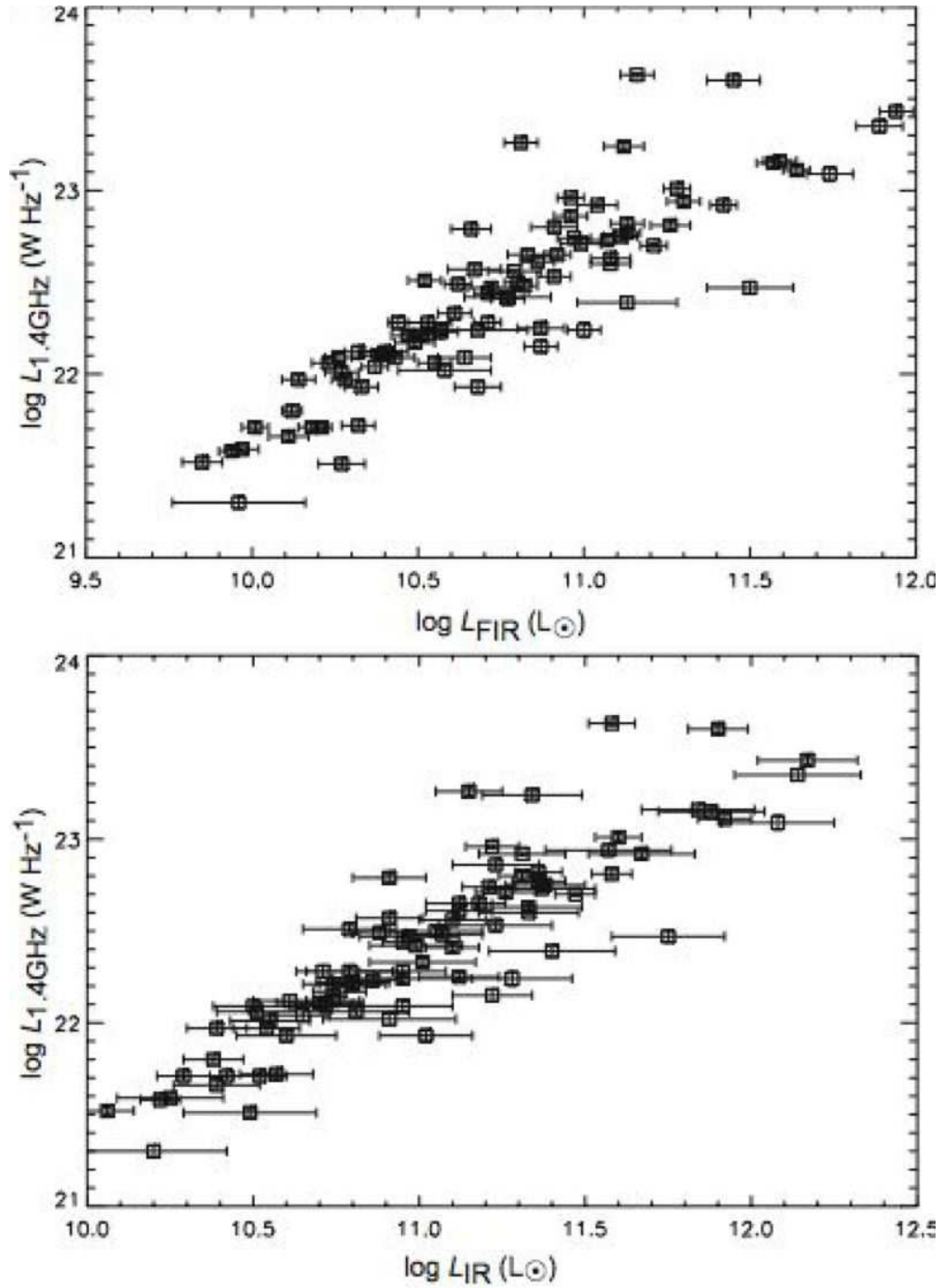


Fig. 5.— Logarithmic plots of the 1.4 GHz radio luminosity vs. FIR luminosity (*top*) and total IR luminosity (*bottom*) of the galaxies in our observed sample. The correlation coefficients are 88% and 89% for the *top* and *bottom* plots, respectively.

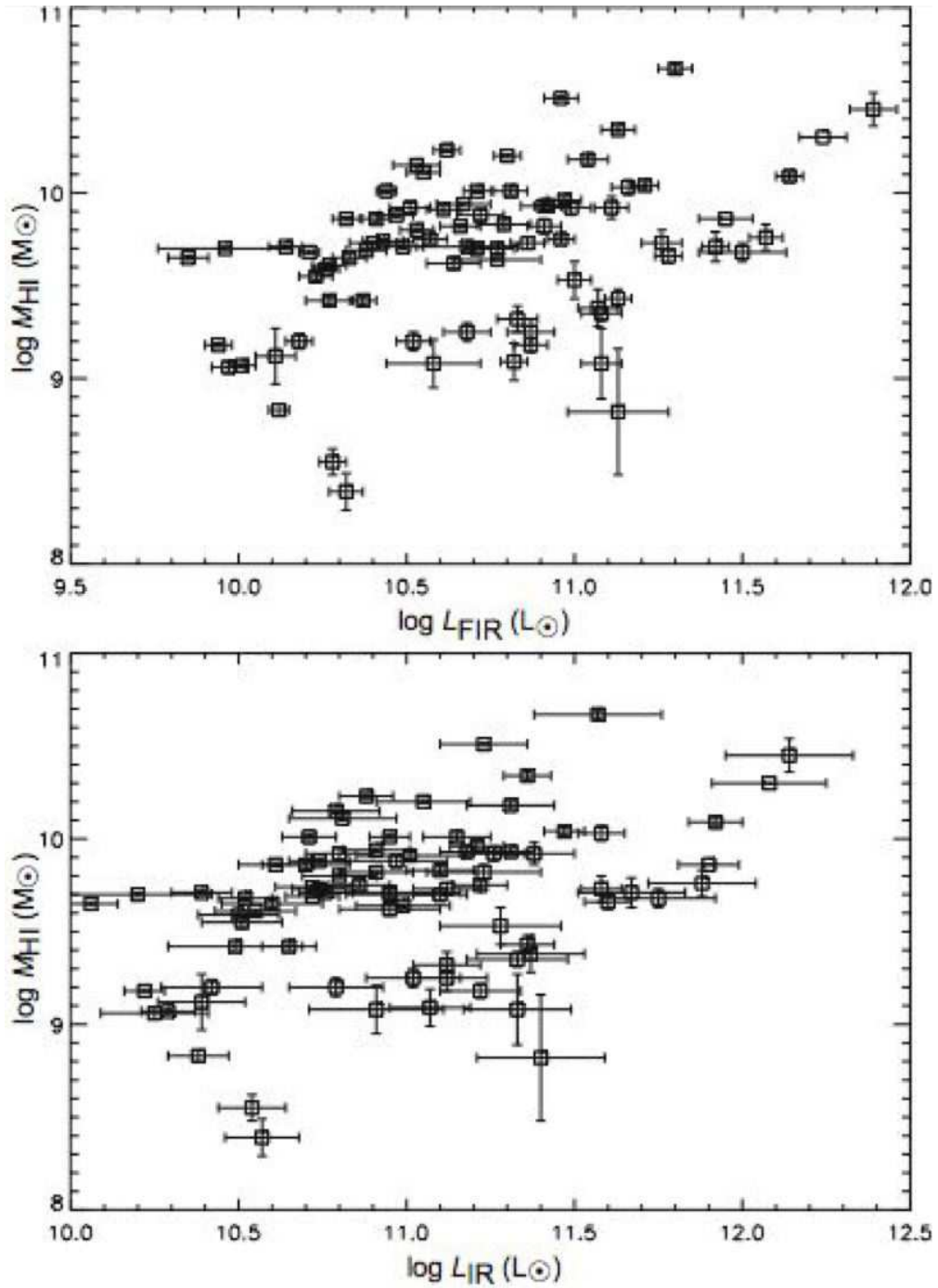


Fig. 6.— Logarithmic plots of the H I mass vs. FIR luminosity (*top*) and total IR luminosity (*bottom*) of the galaxies in our observed sample. The correlation coefficient in each of these plots is 42%.

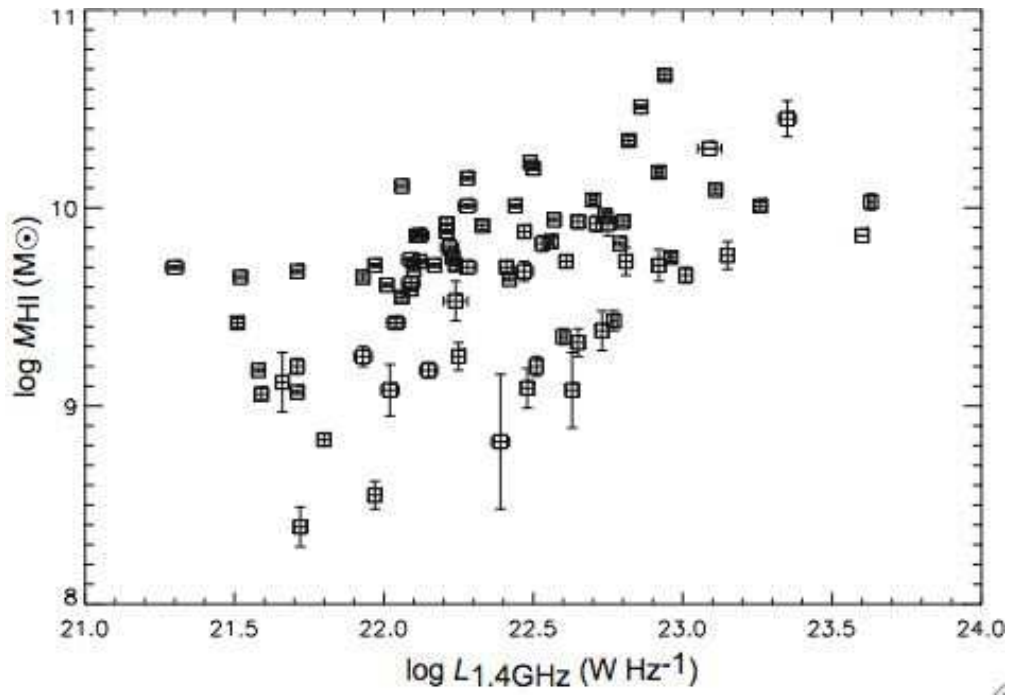


Fig. 7.— Logarithmic plot of the H I mass vs. the 1.4 GHz radio luminosity of the galaxies in our observed sample. The correlation coefficient in this plot is 53%.



Table 1. Sample Properties

IRAS Name	Other Names	R. A. (J2000)	Decl. (J2000)	$z$	$S_{60\mu\text{m}}$ (Jy)	$S_{1.4\text{GHz}}$ (mJy)	Morphology
(1)	(2)	(3)	(4)	(5)	(6)	(7)	(8)
20082+0058		20 10 46.29	+01 07 13.6	0.0258	2.69	5.6	S?
20093+0536	UGC 11522	20 11 49.36	+05 45 47.0	0.0175	3.96	44.9	Sbc
20178-0052		20 20 28.00	-00 42 36.5	0.0185	3.08	21.9	HII
20198+0159		20 22 23.07	+02 09 19.1	0.0414	2.40	14.6	S?
20210+1121		20 23 25.54	+11 31 37.2	0.0564	3.38	53.7	Sy2/Sc
20230+1024		20 25 30.64	+10 34 21.5	0.0260	2.01	8.1	Sbc
20332+0805		20 35 39.16	+08 16 15.8	0.0279	3.11	19.2	HII/S?
20369+0150		20 39 26.45	+02 01 04.1	0.0129	2.41	11.5	Sb/S0-a
20381+0325		20 40 39.34	+03 35 47.7	0.0259	2.07	18.5	
20415+1219	NGC 6956, UGC 11619	20 43 53.46	+12 30 35.4	0.0156	3.18	35.9	SBb
20417+1214	UGC 11620	20 44 09.74	+12 25 05.0	0.0149	2.55	23.4	Sb/S0-a
20480+0937		20 50 29.09	+09 49 05.5	0.0147	2.34	10.9	SABa
20491+1846	UGC 11643	20 51 25.90	+18 58 04.8	0.0291	2.79	23.4	SBb
20550+1656	II Zw 096	20 57 24.14	+17 07 41.2	0.0361	13.30	43.2	HII/S0-a
21052+0340	UGC 11680	21 07 45.88	+03 52 40.5	0.0259	2.80	16.9	Scd/HII Sy2/E-S0
21054+2314		21 07 43.36	+23 27 06.4	0.0487	2.23*	11.6	S?
21116+0158	IC 1368, UGC 11703	21 14 12.57	+02 10 41.2	0.0130	4.03	25.8	Sa;Sy2
21271+0627	NGC 7074, II Zw 133	21 29 38.93	+06 40 57.3	0.0116	3.11	21.7	S?
21278+2629	NGC 7080, UGC 11756	21 30 01.81	+26 43 05.3	0.0161	3.16	28.4	SBb
21396+3623		21 41 41.65	+36 36 47.4	0.1493	2.16*	13.8	
21442+0007		21 46 51.28	+00 21 13.5	0.0740	2.11	10.9	HII
21561+1148	Mrk 0518, UGC 11865	21 58 36.09	+12 02 19.4	0.0311	2.73*	29.1	I?/S?
21582+1018	Mrk 0520, UGC 11871	22 00 41.40	+10 33 07.5	0.0266	4.15	57.9	Sb;Sy1.9
22032+0512		22 05 47.08	+05 27 16.3	0.0383	2.43	5.1	S?
22045+0959	NGC 7212	22 07 02.05	+10 14 02.7	0.0266	2.88	114.1	Sab;Sy2
22171+2908	NGC 7253A, Arp 278, UGC 11984	22 19 27.94	+29 23 41.6	0.0152	5.86	72.1	SABc

Table 1—Continued

IRAS Name	Other Names	R. A. (J2000)	Decl. (J2000)	$z$	$S_{60\mu m}$ (Jy)	$S_{1.4GHz}$ (mJy)	Morphology
(1)	(2)	(3)	(4)	(5)	(6)	(7)	(8)
22217+3310	UGC 12022	22 24 02.76	+33 26 08.9	0.0218	2.25	10.8	Sbc
22221+1748		22 24 33.40	+18 03 56.5	0.0204	2.66	21.0	S-I/Sc
22347+3409	NGC 7331, UGC 12113	22 37 04.67	+34 24 28.0	0.0027	23.10	217.6	SAB;LIN/Sbc
22387+3154	Mrk 0917, UGC 12149	22 41 07.60	+32 10 11.1	0.0244	3.71	33.3	SBa;Sy2
22388+3359	UGC 12150	22 41 12.28	+34 14 57.4	0.0214	8.17	38.3	SB0-a;HII/LIN
22395+2000		22 41 56.03	+20 15 41.6	0.0233	2.56	16.9	Sy2;HII/S0
22402+2914		22 42 38.53	+29 30 23.2	0.0244	2.02	13.4	S?
22449+0757		22 47 28.17	+08 13 37.6	0.0372	2.87	14.0	S?
22472+3439		22 49 32.17	+34 55 09.2	0.0234	4.98	43.9	Sbrst;LIN
22501+2427	Mrk 0309, IV Zw 121	22 52 34.76	+24 43 44.8	0.0421	3.43	7.3	Sa;Sbrst/Sy2
22523+3156		22 54 45.05	+32 12 47.8	0.0212	2.27	32.0	Sb/Sbc
22575+1542	NGC 7448, Arp 013, UGC 12294	23 00 03.60	+15 58 50.8	0.0073	7.23	81.5	SABc/Sc
22586+0523	UGC 12304	23 01 08.21	+05 39 15.8	0.0116	2.06	13.5	Sc
22595+1541	NGC 7465, Mrk 0313, UGC 12317	23 02 00.93	+15 57 51.2	0.0066	3.80	19.1	SB0;Sy2
23007+2329		23 03 09.28	+23 45 32.3	0.0259	3.64	11.9	S?
23007+0836	NGC 7469, Arp 298, Mrk 1514, UGC 12332	23 03 15.62	+08 52 26.1	0.0163	25.90	180.5	SABa/Sy1.2
23011+0046		23 03 41.29	+01 02 38.0	0.0420	2.58	13.3	Sm
23024+1203	NGC 7479, UGC 12343	23 04 56.63	+12 19 20.6	0.0079	12.80	99.0	SBc;LIN/SBbc;Sy1.9
23024+1916		23 04 56.61	+19 33 08.1	0.0251	7.53	42.6	LIN/Sa
23031+1856		23 05 36.16	+19 12 29.6	0.0262	2.09	6.8	Sbrst/Sa
23050+0359		23 07 35.73	+04 15 59.8	0.0474	3.89	15.8	HII/S?
23106+0603	NGC 7518, Mrk 0527, UGC 12422	23 13 12.67	+06 19 23.3	0.0118	4.20	10.7	SABa
23121+0415	NGC 7541, UGC 12447	23 14 44.00	+04 32 00.8	0.0090	19.30	162.4	SBbc;HII
23157+0618	NGC 7591, UGC 12486	23 18 16.32	+06 35 08.5	0.0165	7.22	52.1	SBbc;Sy;LIN
23161+2457	Mrk 0319, UGC 12490	23 18 38.41	+25 13 58.4	0.0270	4.27	31.6	SBa;Sbrst
23176+2356	NGC 7620, Mrk 0321, UGC 12520	23 20 05.65	+24 13 15.9	0.0320	2.41	31.5	Scd;Sbrst/HII

Table 1—Continued

IRAS Name	Other Names	R. A. (J2000)	Decl. (J2000)	$z$	$S_{60\mu m}$ (Jy)	$S_{1.4GHz}$ (mJy)	Morphology
(1)	(2)	(3)	(4)	(5)	(6)	(7)	(8)
23179+2702	NGC 7624, Mrk 0323, UGC 12527	23 20 22.69	+27 18 55.7	0.0143	3.16	24.6	SBc;HII/Sbrst
23179+1657	NGC 7625, Arp 212, III Zw 102, UGC 12529	23 20 30.08	+17 13 32.4	0.0054	9.33	60.3	SAa/HII
23201+0805		23 22 43.92	+08 21 34.7	0.0378	2.33	7.4	Sy2/S?
23204+0601	III Zw 103	23 23 01.60	+06 18 05.8	0.0560	4.23	19.4	HII/S?
23213+0923	NGC 7648, IC 1486, Mrk 0531, UGC 12575	23 23 53.86	+09 40 02.4	0.0119	4.84	16.9	S0
23252+2318	NGC 7673, Mrk 0325, IV Zw 149, UGC 12607	23 27 41.28	+23 35 22.5	0.0114	4.91	43.4	SAC;HII;Sbrst
23254+0830	NGC 7674, Arp 182, Mrk 0533, UGC 12608	23 27 56.70	+08 46 43.2	0.0289	5.59	220.9	SABc;HII;Sy2
23256+2315	NGC 7677, Mrk 0326, UGC 12610	23 28 06.22	+23 31 52.1	0.0119	3.96	16.8	SABbc;Sbrst
23259+2208	NGC 7678, Arp 028, UGC 12614	23 28 27.31	+22 25 07.3	0.0116	6.59	49.5	SABc;Sbrst Sy2
23262+0314	NGC 7679, Arp 216, Mrk 0534, UGC 12618	23 28 46.73	+03 30 41.3	0.0171	7.41*	55.8	SB0;HII;Sy1/SB0-rs;Sy2
23277+1529	UGC 12633	23 30 13.57	+15 45 40.6	0.0141	3.11	23.7	SB/Sbab
23327+2913		23 35 11.88	+29 30 00.3	0.1067	2.10	7.8	LIN
23336+0152	NGC 7714, Arp 284, Mrk 0538, UGC 12699	23 36 14.12	+02 09 18.1	0.0093	10.40	65.8	SBb;HII;LIN
23365+3604		23 39 01.24	+36 21 09.0	0.0645	7.09	27.2	SBa;LIN
23381+2654		23 40 42.78	+27 10 40.9	0.0339	2.17	13.1	Sa/S0
23387+2516		23 41 16.13	+25 33 03.7	0.0314	3.02	37.3	Sb
23410+0228		23 43 39.65	+02 45 06.1	0.0912	2.28	6.0	Sy1/S?
23414+0014	NGC 7738, UGC 12757	23 44 02.01	+00 30 59.5	0.0226	4.47	36.2	SBb
23433+1147	IC 1508, UGC 12773	23 45 55.04	+12 03 42.6	0.0142	3.28	30.1	Sdm/Scd
23446+1519		23 47 09.40	+15 35 49.4	0.0259	4.26	9.2	HII;Sy2/SBab
23456+2056	UGC 12787	23 48 13.77	+21 13 03.5	0.0222	2.29	17.3	Sbc
23471+2939	UGC 12798	23 49 39.73	+29 55 55.1	0.0176	2.47	18.1	S?/Sc
23485+1952	NGC 7769, Mrk 9005, UGC 12808	23 51 04.02	+20 09 00.7	0.0140	4.34	59.9	SAB;HII;LIN
23488+1949	NGC 7771, Mrk 9006, UGC 12815	23 51 24.90	+20 06 41.3	0.0143	19.00	141.4	SBa;HII/Sbrst
23488+2018	Mrk 0331, UGC 12812	23 51 26.79	+20 35 10.6	0.0185	18.60	70.7	HII;Sy2/Sa
23532+2513		23 55 49.99	+25 30 21.9	0.0571	1.44	11.0	HII

Table 1—Continued

IRAS Name	Other Names	R. A. (J2000)	Decl. (J2000)	$z$	$S_{60\mu\text{m}}$ (Jy)	$S_{1.4\text{GHz}}$ (mJy)	Morphology
(1)	(2)	(3)	(4)	(5)	(6)	(7)	(8)
23560+1026	NGC 7794, UGC 12872	23 58 34.09	+10 43 42.2	0.0176	3.26	24.8	S?/Sbc
23564+1833	UGC 12879	23 59 01.32	+18 50 05.0	0.0180	2.64	18.2	S?/Sc
23568+2028	NGC 7798, Mrk 0332, UGC 12884	23 59 25.60	+20 45 00.1	0.0080	4.87	36.5	SBc/Sbrst
23587+1249	NGC 7803, UGC 12906	00 01 19.87	+13 06 40.5	0.0179	2.02	12.3	S0-a
23591+2312	III Zw 125	00 01 40.44	+23 29 34.0	0.0145	6.13	131.9	SBc;Sbrst;LIN
23594+3622		00 01 58.39	+36 38 56.3	0.0321	4.48	75.0	Sy2/S0-a
23597+1241	NGC 7810, UGC 12919	00 02 19.08	+12 58 18.0	0.0185	3.39	23.0	S0

\*The 60  $\mu\text{m}$  values taken from the IRAS Point Source Catalogue (PSC) instead of the IRAS Faint Source Catalogue (FSC).

Table 2. Parameters of Galaxies with H I Emission

IRAS Name	$\Delta t$	rms	$V_{\text{HI}}$	$\Delta V_{50}$	$\int S dv$	$D_L$	$\log \frac{L_{\text{FIR}}}{L_{\odot}}$	$\log \frac{L_{\text{IR}}}{L_{\odot}}$	$\log \frac{M_{\text{HI}}}{M_{\odot}}$
(1)	(min)	(mJy)	( $\text{km s}^{-1}$ )	( $\text{km s}^{-1}$ )	( $\text{Jy km s}^{-1}$ )	(Mpc)	(8)	(9)	(10)
20082+0058	15	0.30	$7784.6 \pm 3.5$	$275.1 \pm 7.0$	$0.6 \pm 0.1$	$111.9 \pm 0.1$	$10.68 \pm 0.07$	$11.02 \pm 0.14$	$9.25 \pm 0.05$
20093+0536	15	0.33	$5286.5 \pm 0.8$	$323.5 \pm 1.6$	$12.6 \pm 0.1$	$75.5 \pm < 0.1$	$10.62 \pm 0.04$	$10.88 \pm 0.08$	$10.23 \pm < 0.01$
20178-0052 $^{\circ}$	5	0.90	$5520.0 \pm 3.2$	$317.6 \pm 6.4$	$5.6 \pm 0.4$	$78.9 \pm 0.1$	$10.51 \pm 0.06$	$10.80 \pm 0.10$	$9.92 \pm 0.03$
20198+0159	20	0.37	$12301.0 \pm 3.6$	$394.8 \pm 7.3$	$1.1 \pm 0.1$	$178.8 \pm 0.1$	$11.11 \pm 0.05$	$11.38 \pm 0.12$	$9.92 \pm 0.06$
20210+1121*	10	0.41	$16905.0 \pm 25.0$	400.0	0.5	$248.7 \pm 0.4$	$11.45 \pm 0.08$	$11.90 \pm 0.09$	$< 9.86$
20230+1024	15	0.27	$7811.3 \pm 2.4$	$222.1 \pm 4.7$	$1.4 \pm 0.1$	$112.3 \pm < 0.1$	$10.64 \pm 0.08$	$10.95 \pm 0.15$	$9.62 \pm 0.03$
20332+0805	20	0.26	$7967.3 \pm 8.9$	$326.1 \pm 17.9$	$0.4 \pm 0.1$	$114.6 \pm 0.2$	$10.82 \pm 0.04$	$11.07 \pm 0.12$	$9.09 \pm 0.1$
20369+0150	10	0.96	$4027.5 \pm 13.0$	$430.7 \pm 26.0$	$1.7 \pm 0.5$	$57.3 \pm 0.2$	$10.11 \pm 0.06$	$10.39 \pm 0.13$	$9.12 \pm 0.15$
20381+0325	10	0.37	$8037.5 \pm 4.1$	$486.7 \pm 8.1$	$2.4 \pm 0.2$	$115.6 \pm 0.1$	$10.72 \pm 0.07$	$10.97 \pm 0.15$	$9.88 \pm 0.03$
20415+1219	5	0.49	$4640.8 \pm 1.3$	$361.3 \pm 2.6$	$9.9 \pm 0.2$	$66.2 \pm 0.1$	$10.44 \pm 0.03$	$10.71 \pm 0.08$	$10.01 \pm 0.01$
20417+1214	10	0.42	$4483.7 \pm 3.4$	$364.5 \pm 6.9$	$3.7 \pm 0.2$	$63.9 \pm < 0.1$	$10.23 \pm 0.05$	$10.51 \pm 0.12$	$9.55 \pm 0.02$
20480+0937	5	0.46	$4391.2 \pm 2.1$	$329.2 \pm 4.3$	$1.7 \pm 0.2$	$62.6 \pm 0.1$	$10.18 \pm 0.04$	$10.42 \pm 0.15$	$9.20 \pm 0.04$
20491+1846	10	0.31	$8715.1 \pm 5.7$	$504.3 \pm 11.3$	$2.3 \pm 0.1$	$125.6 \pm 0.1$	$10.92 \pm 0.04$	$11.18 \pm 0.08$	$9.93 \pm 0.03$
20550+1656	10	0.29	$10824.7 \pm 1.9$	$282.0 \pm 3.8$	$2.1 \pm 0.1$	$156.8 \pm < 0.1$	$11.64 \pm 0.04$	$11.92 \pm 0.08$	$10.09 \pm 0.02$
21052+0340	15	0.27	$7792.3 \pm 3.6$	$518.2 \pm 7.2$	$1.7 \pm 0.1$	$112.0 \pm 0.1$	$10.77 \pm 0.05$	$11.10 \pm 0.08$	$9.70 \pm 0.03$
21054+2314 $^{\dagger}$	15	0.28	$14667.6 \pm 3.5$	$207.6 \pm 7.1$	$0.5 \pm 0.1$	$214.5 \pm 0.1$	$11.26 \pm 0.06$	$11.58 \pm 0.06$	$9.73 \pm 0.07$
21116+0158 $^{\dagger}$	20	0.21	$3847.7 \pm 5.3$	$519.2 \pm 10.7$	$0.5 \pm 0.1$	$54.7 \pm 0.1$	$10.28 \pm 0.04$	$10.54 \pm 0.10$	$8.55 \pm 0.07$
21271+0627	10	0.25	$3454.2 \pm 3.3$	$262.3 \pm 6.6$	$1.2 \pm 0.1$	$49.1 \pm 0.1$	$10.12 \pm 0.03$	$10.38 \pm 0.09$	$8.83 \pm 0.03$
21278+2629	20	0.63	$4837.0 \pm 0.6$	$157.1 \pm 1.3$	$6.8 \pm 0.2$	$69.0 \pm < 0.1$	$10.47 \pm 0.05$	$10.74 \pm 0.09$	$9.88 \pm 0.01$
21561+1148	15	0.20	$9343.9 \pm 1.3$	$240.7 \pm 2.6$	$2.0 \pm 0.1$	$134.8 \pm 0.1$	$10.91 \pm 0.07$	$11.31 \pm 0.07$	$9.93 \pm 0.02$
21582+1018 $^{\dagger}$	20	0.22	$7972.3 \pm 1.4$	$295.4 \pm 2.7$	$1.8 \pm 0.1$	$114.6 \pm 0.1$	$10.96 \pm 0.04$	$11.22 \pm 0.08$	$9.75 \pm 0.02$
22032+0512	20	0.31	$11638.4 \pm 9.2$	$357.1 \pm 18.5$	$0.5 \pm 0.1$	$168.9 \pm 0.2$	$11.00 \pm 0.05$	$11.28 \pm 0.18$	$9.53 \pm 0.10$
22045+0959 $^{\dagger \circ}$	20	0.21	$7981.3 \pm 4.8$	$563.3 \pm 9.7$	$3.3 \pm 0.2$	$114.8 \pm 0.3$	$10.81 \pm 0.05$	$11.15 \pm 0.10$	$10.01 \pm 0.02$
22171+2908	10	0.45	$4581.8 \pm 0.9$	$442.8 \pm 1.8$	$8.7 \pm 0.2$	$65.3 \pm < 0.1$	$10.67 \pm 0.08$	$10.91 \pm 0.10$	$9.94 \pm 0.01$
22217+3310	10	0.35	$6528.5 \pm 0.7$	$437.4 \pm 1.4$	$6.3 \pm 0.1$	$93.5 \pm < 0.1$	$10.55 \pm 0.05$	$10.81 \pm 0.16$	$10.11 \pm 0.01$
22221+1748	10	0.33	$6098.5 \pm 1.1$	$358.1 \pm 2.2$	$7.8 \pm 0.1$	$87.3 \pm < 0.1$	$10.53 \pm 0.07$	$10.79 \pm 0.13$	$10.15 \pm 0.01$
22347+3409 $^{\circ}$	10	0.54	$800.4 \pm 0.1$	$508.1 \pm 0.3$	$148.1 \pm 0.3$	$11.3 \pm < 0.1$	$9.85 \pm 0.06$	$10.06 \pm 0.08$	$9.65 \pm < 0.01$
22387+3154	10	0.36	$7326.1 \pm 6.5$	$316.9 \pm 13.1$	$0.8 \pm 0.1$	$105.2 \pm 0.1$	$10.83 \pm 0.06$	$11.12 \pm 0.10$	$9.32 \pm 0.07$
22388+3359	20	0.27	$6480.6 \pm 4.6$	$345.7 \pm 9.2$	$1.1 \pm 0.1$	$92.8 \pm 0.1$	$11.08 \pm 0.06$	$11.33 \pm 0.15$	$9.35 \pm 0.04$
22395+2000	10	0.39	$7144.6 \pm 2.8$	$426.0 \pm 5.6$	$3.3 \pm 0.2$	$102.5 \pm 0.1$	$10.61 \pm 0.05$	$11.01 \pm 0.16$	$9.91 \pm 0.02$
22402+2914	20	0.26	$7258.9 \pm 1.4$	$602.5 \pm 2.8$	$2.0 \pm 0.1$	$104.2 \pm < 0.1$	$10.68 \pm 0.15$	$10.95 \pm 0.21$	$9.71 \pm 0.02$
22449+0757	25	0.23	$11040.4 \pm 20.2$	$348.2 \pm 40.4$	$0.2 \pm 0.1$	$160.0 \pm 0.3$	$11.08 \pm 0.06$	$11.33 \pm 0.16$	$9.08 \pm 0.19$
22472+3439	10	0.36	$7107.0 \pm 1.5$	$463.5 \pm 3.0$	$3.7 \pm 0.1$	$102.0 \pm < 0.1$	$10.97 \pm 0.05$	$11.21 \pm 0.08$	$9.96 \pm 0.02$

Table 2—Continued

IRAS Name	$\Delta t$	rms	$V_{\text{HI}}$	$\Delta V_{50}$	$\int S dv$	$D_L$	$\log \frac{L_{\text{FIR}}}{L_{\odot}}$	$\log \frac{L_{\text{IR}}}{L_{\odot}}$	$\log \frac{M_{\text{HI}}}{M_{\odot}}$
(1)	(min) (2)	(mJy) (3)	(km s <sup>-1</sup> ) (4)	(km s <sup>-1</sup> ) (5)	(Jy km s <sup>-1</sup> ) (6)	(Mpc) (7)	(8)	(9)	(10)
22501+2427	20	0.25	12641.0 ± 1.7	220.5 ± 3.5	0.6 ± 0.1	183.9 ± 0.1	11.50 ± 0.13	11.75 ± 0.17	9.68 ± 0.05
22523+3156 <sup>†</sup>	25	0.23	6373.9 ± 11.3	724.8 ± 22.7	0.8 ± 0.1	91.3 ± 0.2	10.52 ± 0.05	10.79 ± 0.14	9.20 ± 0.05
22575+1542	5	0.58	2190.6 ± 0.3	293.3 ± 0.5	22.8 ± 0.2	31.0 ± < 0.1	10.14 ± 0.05	10.39 ± 0.09	9.71 ± < 0.01
22586+0523	10	0.34	3461.8 ± 2.3	297.9 ± 4.6	2.0 ± 0.1	49.2 ± < 0.1	9.97 ± 0.05	10.25 ± 0.16	9.06 ± 0.03
22595+1541	5	0.60	2089.6 ± 0.5	692.1 ± 1.0	24.2 ± 0.2	29.6 ± < 0.1	9.96 ± 0.20	10.20 ± 0.22	9.70 ± < 0.01
23007+2329	10	0.29	7758.9 ± 5.8	215.2 ± 11.6	0.6 ± 0.1	111.5 ± 0.1	10.87 ± 0.07	11.12 ± 0.12	9.25 ± 0.07
23007+0836 <sup>†◊</sup>	15	0.47	4808.3 ± 5.6	550.4 ± 11.2	2.3 ± 0.2	68.6 ± 0.3	11.28 ± 0.04	11.60 ± 0.07	9.66 ± 0.04
23011+0046	15	0.35	12666.5 ± 5.8	160.3 ± 11.7	0.3 ± 0.1	184.3 ± 0.1	11.07 ± 0.06	11.37 ± 0.16	9.38 ± 0.10
23024+1203 <sup>◊</sup>	10	0.37	2352.2 ± 0.5	366.3 ± 1.0	20.5 ± 0.2	33.3 ± 0.1	10.40 ± 0.07	10.74 ± 0.08	9.73 ± 0.01
23024+1916	15	0.31	7453.8 ± 3.4	419.3 ± 6.8	1.0 ± 0.1	107.0 ± 0.1	11.13 ± 0.04	11.36 ± 0.08	9.43 ± 0.05
23031+1856	15	0.29	7864.1 ± 10.8	425.2 ± 21.7	0.4 ± 0.1	113.1 ± 0.2	10.58 ± 0.14	10.91 ± 0.20	9.08 ± 0.13
23050+0359	20	0.28	14258.4 ± 8.1	321.3 ± 16.3	0.5 ± 0.1	208.3 ± 0.1	11.42 ± 0.04	11.67 ± 0.16	9.71 ± 0.08
23106+0603 <sup>◊</sup>	10	0.53	3530.3 ± 0.9	97.0 ± 1.7	4.4 ± 0.2	50.2 ± < 0.1	10.27 ± 0.07	10.49 ± 0.20	9.42 ± 0.02
23121+0415 <sup>◊</sup>	5	0.61	2655.6 ± 0.4	455.5 ± 0.8	30.2 ± 0.3	37.7 ± < 0.1	10.71 ± 0.04	10.95 ± 0.06	10.01 ± < 0.01
23157+0618	5	0.66	4952.6 ± 0.7	419.2 ± 1.4	13.5 ± 0.3	70.7 ± < 0.1	10.80 ± 0.04	11.05 ± 0.14	10.20 ± 0.01
23161+2457	5	0.75	8114.3 ± 4.7	242.0 ± 9.3	2.6 ± 0.2	116.7 ± 0.1	10.99 ± 0.06	11.26 ± 0.09	9.92 ± 0.04
23176+2356	5	0.49	9582.6 ± 0.8	257.7 ± 1.6	7.2 ± 0.2	138.4 ± < 0.1	10.96 ± 0.05	11.23 ± 0.13	10.51 ± 0.01
23179+2702	10	0.32	4272.1 ± 1.4	306.1 ± 2.8	3.0 ± 0.1	60.9 ± 0.1	10.37 ± 0.04	10.65 ± 0.08	9.42 ± 0.02
23179+1657	5	0.45	1628.5 ± 0.5	210.8 ± 1.1	12.0 ± 0.1	23.0 ± < 0.1	9.94 ± 0.04	10.22 ± 0.06	9.18 ± 0.01
23201+0805	20	0.28	11502.1 ± 12.7	122.6 ± 25.4	0.1 ± 0.1	166.9 ± 0.2	11.13 ± 0.15	11.40 ± 0.19	8.82 ± 0.34
23204+0601	20	0.16	16725.6 ± 4.1	350.9 ± 8.2	0.4 ± 0.1	245.9 ± 0.1	11.57 ± 0.05	11.88 ± 0.16	9.76 ± 0.07
23213+0923	15	0.28	3580.7 ± 3.8	347.2 ± 7.5	0.4 ± 0.1	50.9 ± 0.1	10.32 ± 0.05	10.57 ± 0.11	8.39 ± 0.10
23252+2318	5	0.59	3404.2 ± 0.7	181.0 ± 1.3	7.0 ± 0.2	48.4 ± < 0.1	10.26 ± 0.04	10.50 ± 0.12	9.59 ± 0.01
23254+0830 <sup>†◊</sup>	5	0.73	8833.1 ± 2.7	452.1 ± 5.5	2.8 ± 0.3	127.3 ± < 0.1	11.16 ± 0.05	11.58 ± 0.07	10.03 ± 0.04
23256+2315	5	0.58	3555.3 ± 0.5	277.7 ± 1.1	8.0 ± 0.2	50.5 ± 0.1	10.21 ± 0.03	10.52 ± 0.08	9.68 ± 0.01
23259+2208	5	0.51	3488.2 ± 0.6	306.8 ± 1.2	8.9 ± 0.2	49.6 ± < 0.1	10.49 ± 0.06	10.76 ± 0.08	9.71 ± 0.01
23262+0314	5	0.56	5141.8 ± 1.3	299.1 ± 2.7	5.3 ± 0.2	73.4 ± < 0.1	10.79 ± 0.08	11.10 ± 0.10	9.83 ± 0.02
23277+1529	5	0.41	4219.5 ± 1.3	322.5 ± 2.6	4.8 ± 0.2	60.1 ± < 0.1	10.27 ± 0.05	10.55 ± 0.12	9.61 ± 0.01
23327+2913	45	0.28	32145.4 ± 3.9	488.6 ± 7.7	0.5 ± 0.1	490.1 ± 0.1	11.89 ± 0.07	12.14 ± 0.19	10.45 ± 0.09
23336+0152	5	0.73	2795.6 ± 0.6	214.6 ± 1.2	13.3 ± 0.2	39.7 ± < 0.1	10.38 ± 0.06	10.72 ± 0.08	9.69 ± 0.01
23381+2654	10	0.35	10177.0 ± 4.7	302.1 ± 9.4	1.3 ± 0.1	147.2 ± 0.1	10.91 ± 0.05	11.23 ± 0.17	9.82 ± 0.04
23387+2516	10	0.41	9403.5 ± 2.1	465.0 ± 4.2	3.5 ± 0.2	135.7 ± 0.1	11.04 ± 0.06	11.31 ± 0.13	10.18 ± 0.02
23410+0228*	20	0.40	27335.0 ± 96.0	400.0	0.5	412.3 ± 1.6	11.74 ± 0.07	12.08 ± 0.17	< 10.30

Table 2—Continued

IRAS Name	$\Delta t$	rms	$V_{\text{HI}}$	$\Delta V_{50}$	$\int S dv$	$D_L$	$\log \frac{L_{\text{FIR}}}{L_{\odot}}$	$\log \frac{L_{\text{IR}}}{L_{\odot}}$	$\log \frac{M_{\text{HI}}}{M_{\odot}}$
(1)	(min)	(mJy)	( $\text{km s}^{-1}$ )	( $\text{km s}^{-1}$ )	( $\text{Jy km s}^{-1}$ )	(Mpc)	(8)	(9)	(10)
(2)	(3)	(4)	(5)	(6)	(7)	(8)	(9)	(10)	
23414+0014	10	0.42	$6762.8 \pm 2.5$	$436.5 \pm 4.9$	$2.4 \pm 0.2$	$97.0 \pm 0.1$	$10.86 \pm 0.05$	$11.12 \pm 0.10$	$9.73 \pm 0.03$
23433+1147	5	0.66	$4262.5 \pm 0.9$	$322.2 \pm 1.9$	$8.4 \pm 0.3$	$60.7 \pm < 0.1$	$10.32 \pm 0.04$	$10.61 \pm 0.11$	$9.86 \pm 0.01$
23446+1519	10	0.25	$7864.3 \pm 1.6$	$91.0 \pm 3.2$	$0.5 \pm 0.0$	$113.1 \pm 0.1$	$10.87 \pm 0.05$	$11.22 \pm 0.12$	$9.18 \pm 0.04$
23456+2056	10	0.35	$6673.1 \pm 2.7$	$457.0 \pm 5.4$	$2.3 \pm 0.1$	$95.6 \pm 0.1$	$10.71 \pm 0.04$	$10.95 \pm 0.13$	$9.70 \pm 0.03$
23471+2939	10	0.30	$5268.8 \pm 1.2$	$402.1 \pm 2.3$	$4.4 \pm 0.1$	$75.2 \pm 0.1$	$10.43 \pm 0.06$	$10.72 \pm 0.11$	$9.74 \pm 0.01$
23485+1952	5	0.41	$4227.6 \pm 1.6$	$347.7 \pm 3.2$	$5.1 \pm 0.2$	$60.2 \pm < 0.1$	$10.77 \pm 0.13$	$10.99 \pm 0.14$	$9.64 \pm 0.01$
23488+1949 <sup>◊</sup>	5	1.37	$4362.5 \pm 5.3$	$815.4 \pm 10.6$	$23.7 \pm 1.0$	$62.2 \pm 0.1$	$11.13 \pm 0.05$	$11.36 \pm 0.07$	$10.34 \pm 0.02$
23488+2018 <sup>◊</sup>	10	0.45	$5392.5 \pm 1.7$	$346.8 \pm 3.5$	$7.9 \pm 0.3$	$77.0 \pm 0.1$	$11.21 \pm 0.04$	$11.47 \pm 0.06$	$10.04 \pm 0.02$
23532+2513	30	0.20	$17395.3 \pm 3.5$	$784.5 \pm 7.0$	$3.0 \pm 0.1$	$256.1 \pm 0.1$	$11.30 \pm 0.05$	$11.57 \pm 0.19$	$10.67 \pm 0.02$
23560+1026	5	0.25	$5227.1 \pm 0.7$	$302.0 \pm 1.4$	$4.8 \pm 0.1$	$74.6 \pm < 0.1$	$10.53 \pm 0.05$	$10.80 \pm 0.11$	$9.80 \pm 0.01$
23564+1833	5	0.50	$5375.4 \pm 1.1$	$319.6 \pm 2.2$	$5.2 \pm 0.2$	$76.8 \pm < 0.1$	$10.41 \pm 0.04$	$10.70 \pm 0.13$	$9.86 \pm 0.02$
23568+2028	5	0.49	$2402.4 \pm 0.5$	$109.9 \pm 1.0$	$4.3 \pm 0.1$	$34.1 \pm 0.1$	$10.01 \pm 0.04$	$10.29 \pm 0.08$	$9.07 \pm 0.01$
23587+1249	5	0.38	$5317.2 \pm 4.0$	$357.5 \pm 7.9$	$3.3 \pm 0.2$	$75.9 \pm 0.1$	$10.33 \pm 0.05$	$10.60 \pm 0.15$	$9.65 \pm 0.02$
23591+2312 <sup>◊</sup>	5	0.51	$4366.1 \pm 1.8$	$627.5 \pm 3.5$	$7.3 \pm 0.2$	$62.2 \pm < 0.1$	$10.66 \pm 0.06$	$10.91 \pm 0.11$	$9.82 \pm 0.01$
23597+1241	10	0.33	$5487.7 \pm 1.4$	$417.7 \pm 2.9$	$3.9 \pm 0.1$	$78.4 \pm < 0.1$	$10.57 \pm 0.05$	$10.86 \pm 0.09$	$9.75 \pm 0.02$

<sup>◊</sup>Sources observed in DPS mode.

\*HI 21 cm non-detections.

<sup>†</sup>Sources that exhibit both emission and absorption features, but with parameters derived from the emission part of the spectra. The flux density integrals and neutral hydrogen masses should be considered lower limits since some of the emission might be masked by absorption features.

Table 3. Parameters of Galaxies with H I Absorption

IRAS Name	$D_L^a$ (Mpc)	$\log \frac{L_{\text{FIR}}}{L_\odot}$	$\log \frac{L_{\text{IR}}}{L_\odot}$	$\Delta t$ (min)	rms (mJy)	$V_{\text{HI-Peak}}$ (km s $^{-1}$ )	$\Delta V_{50}$ (km s $^{-1}$ )	$\tau_{\text{max}} \times 10^{-2}$	$N_{\text{HI}}/T_s \times 10^{18}$ (cm $^{-2}$ K $^{-1}$ )
(1)	(2)	(3)	(4)	(5)	(6)	(7)	(8)	(9)	(10)
21054+2314 $^\dagger$	$214.5 \pm 0.1$	$11.26 \pm 0.06$	$11.58 \pm 0.06$	15	0.28	$14893 \pm 9$	$144 \pm 24$	$7.1 \pm 0.2$	$12.6 \pm 0.4$
21116+0158 $^\dagger$	$54.7 \pm 0.1$	$10.28 \pm 0.04$	$10.54 \pm 0.10$	20	0.21	$4079 \pm 11$	$94 \pm 9$	$17.9 \pm 1.8$	$19.5 \pm 0.7$
21442+0007	$330.9 \pm 0.4$	$11.59 \pm 0.05$	$11.84 \pm 0.17$	25	0.31	$22241 \pm 6$	$101 \pm 21$	$11.0 \pm 2.2$	$15.3 \pm 0.9$
21582+1018 $^\dagger$	$114.6 \pm 0.1$	$10.96 \pm 0.04$	$11.22 \pm 0.08$	20	0.22	$8155 \pm 11$	$141 \pm 40$	$4.0 \pm 0.5$	$4.1 \pm 0.2$
22045+0959 $^\diamond$	$114.8 \pm 0.3$	$10.81 \pm 0.05$	$11.15 \pm 0.10$	20	0.21	$7982 \pm 3$	$62 \pm 20$	$6.1 \pm 0.6$	$7.9 \pm 0.3$
22523+3156 $^\dagger$	$91.3 \pm 0.2$	$10.52 \pm 0.05$	$10.79 \pm 0.14$	25	0.23	$6260 \pm 8$	$185 \pm 20$	$33.8 \pm 1.3$	$44.0 \pm 0.7$
23007+0836 $^\diamond$	$68.6 \pm 0.3$	$11.28 \pm 0.04$	$11.60 \pm 0.07$	15	0.47	$4916 \pm 16$	$75 \pm 5$	$7.2 \pm 0.4$	$9.5 \pm 0.2$
23254+0830 $^\diamond$	$127.3 \pm < 0.1$	$11.16 \pm 0.05$	$11.58 \pm 0.07$	5	0.73	$8571 \pm 8$	$63 \pm 4$	$7.6 \pm 0.3$	$17.9 \pm 0.2$
23365+3604	$286.1 \pm 0.2$	$11.94 \pm 0.05$	$12.17 \pm 0.15$	25	0.30	$19380 \pm 6$	$91 \pm 8$	$9.2 \pm 0.8$	$23.8 \pm 0.5$
23594+3622 $^{\diamond b}$	$139.0 \pm 0.6$	$11.11 \pm 0.06$	$11.34 \pm 0.15$	15	0.62	$9670 \pm 6$	$162 \pm 58$	$6.1 \pm 0.8$	$16.1 \pm 0.5$

$^\diamond$ Sources observed in DPS mode.

$^\dagger$ Sources that exhibit both emission and absorption features, but with H I parameters derived from the absorption part of the spectra.

<sup>a</sup>Derived using the H I emission velocity (Table 2) for sources that exhibit both H I emission and absorption, and optical redshifts (Table 1) for sources that exhibit H I absorption only.

<sup>b</sup>The H I spectrum for this source (Figure 2) shows another weak absorption-like features at 9350 km s $^{-1}$ . However, it only has a  $2.5\sigma$  significance.



Table 4. Parameters of Galaxies with OH Megamaser Emission

IRAS Name	$\Delta t$ (min)	rms (mJy)	1667 MHz				1665 MHz			$R_H$	$\log \frac{L_{\text{OH}}^{\text{pred}}}{L_{\odot}}$	$\log \frac{L_{\text{OH}}}{L_{\odot}}$	$\frac{r_{\text{rms1612}}}{\text{AU}}$ (mJy)	rms <sub>1720</sub> (mJy)
			$V$ (km s <sup>-1</sup> )	$F_{\text{peak}}$ (mJy)	$\Delta V_{50}$ (km s <sup>-1</sup> )	$\int S dv$ (Jy km s <sup>-1</sup> )	$F_{\text{peak}}$ (mJy)	$\Delta V_{50}$ (km s <sup>-1</sup> )	$\int S dv$ (Jy km s <sup>-1</sup> )					
(1)	(2)	(3)	(4)	(5)	(6)	(7)	(8)	(9)	(10)	(11)	(12)	(13)	(14)	(15)
23050+0359	20	0.19	14239 ± 9.6	4.0 ± 0.3	197 ± 13	0.50 ± 0.01	2.0 ± 0.3	200 ± 50	0.24 ± 0.01	2.08 ± 0.10	1.74	1.69	–	–
23327+2913	45	0.19	32285 ± 5.4	1.4 ± 0.2	204 ± 34	0.30 ± 0.01	–	–	–	–	2.39	2.04	0.23	–
23365+3604	25	0.28	19222 ± 7.4	7.1 ± 0.3	256 ± 56	1.90 ± 0.01	2.4 ± 0.3	172 ± 70	0.50 ± 0.01	3.80 ± 0.08	2.46	2.46	0.21	–

Table 5. Parameters of Galaxies with OH Absorption

IRAS Name	$\Delta t$ (min)	rms (mJy)	1667 MHz					1665 MHz			$R_H$	rms <sub>1612</sub> (mJy)	rms <sub>1720</sub> (mJy)
			$V$ (km s <sup>-1</sup> )	$\Delta V_{50}$ (km s <sup>-1</sup> )	$\tau \times 10^{-2}$	$\int \tau dv$ (km s <sup>-1</sup> )	$N_{OH}/T_{ex} \times 10^{14}$ (cm <sup>-2</sup> K <sup>-1</sup> )	$\Delta V_{50}$ (km s <sup>-1</sup> )	$\tau \times 10^{-2}$	$\int \tau dv$ (km s <sup>-1</sup> )			
(1)	(2)	(3)	(4)	(5)	(6)	(7)	(8)	(9)	(10)	(11)	(12)	(13)	(14)
21054+2314	40	0.68	14792 ± 27	133 ± 14	6.5 ± 1.0	7.4 ± 0.3	17.4 ± 0.7	–	–	–	–	–	0.31
22523+3156	25	0.22	6250 ± 2	110 ± 24	16.9 ± 0.6	13.0 ± 0.1	30.6 ± 0.3	76 ± 3	11.0 ± 0.5	6.9 ± 0.1	1.88 ± 0.03	–	0.18
23007+0836	15	0.85	4947 ± 16	200 ± 100	2.1 ± 0.3	4.4 ± 0.1	10.3 ± 0.2	98 ± 51	1.9 ± 0.3	2.3 ± 0.1	1.91 ± 0.09	–	0.18
23121+0415	5	0.72	2650 ± 9	218 ± 68	2.3 ± 0.5	2.4 ± 0.1	5.6 ± 0.3	108 ± 65	2.4 ± 0.5	2.7 ± 0.1	0.89 ± 0.05	0.69	–

Table 6. Parameters of Galaxies with OH Nondetections

IRAS Name	rms <sub>1667,1665</sub> (mJy)	$\log \frac{L_{\text{OH}}^{\text{pred}}}{L_{\odot}}$	$\log \frac{L_{\text{OH}}^{\text{max}}}{L_{\odot}}$	rms <sub>1612</sub> (mJy)	rms <sub>1720</sub> (mJy)
(1)	(2)	(3)	(4)	(5)	(6)
20082+0058	-	0.71	-	-	-
20093+0536	0.31	0.64	-0.17	0.24	-
20178-0052	0.91	0.48	0.34	-	-
20198+0159	-	1.31	-	-	0.30
20210+1121	-	1.78	-	-	-
20230+1024	-	0.66	-	-	0.24
20332+0805	-	0.91	-	0.38	0.42
20369+0150	1.00	-0.07	0.10	0.80	-
20381+0325	-	0.77	-	-	0.25
20415+1219	0.39	0.39	-0.18	0.40	0.52
20417+1214	0.32	0.09	-0.30	0.31	-
20480+0937	0.44	0.03	-0.17	0.45	0.46
20491+1846	-	1.05	-	-	0.27
20550+1656	0.24	2.04	0.35	-	0.23
21052+0340	-	0.84	-	-	0.23
21116+0158	-	0.17	-	0.22	0.14
21271+0627	0.28	-0.06	-0.58	0.23	-
21278+2629	0.46	0.43	-0.07	0.23	0.49
21442+0007	-	1.98	-	0.34	-
21561+1148	0.30	1.03	0.31	0.26	0.26
21582+1018	-	1.10	-	-	0.28
22032+0512	-	1.17	-	-	0.23
22045+0959	-	0.90	-	-	0.79
22171+2908	0.40	0.71	-0.18	0.41	-
22217+3310	-	0.53	-	-	0.33
22221+1748	0.36	0.51	0.03	-	0.53
22347+3409	0.95	-0.42	-1.33	-	-
22387+3154	-	0.93	-	-	0.30
22388+3359	0.35	1.27	0.06	-	0.24

Table 6—Continued

IRAS Name	rms <sub>1667,1665</sub> (mJy)	$\log \frac{L_{\text{OH}}^{\text{pred}}}{L_{\odot}}$	$\log \frac{L_{\text{OH}}^{\text{max}}}{L_{\odot}}$	rms <sub>1612</sub> (mJy)	rms <sub>1720</sub> (mJy)
(1)	(2)	(3)	(4)	(5)	(6)
22395+2000	-	0.62	-	-	0.32
22402+2914	-	0.72	-	-	0.15
22449+0757	-	1.27	-	-	0.16
22472+3439	-	1.12	-	-	0.33
22501+2427	-	1.85	-	-	0.17
22575+1542	0.69	-0.03	-0.59	-	-
22586+0523	0.27	-0.27	-0.60	0.39	0.42
22595+1541	0.51	-0.27	-0.76	-	0.79
23007+2329	-	0.97	-	-	0.29
23011+0046	-	1.26	-	-	0.21
23024+1203	0.36	0.33	-0.81	-	-
23024+1916	-	1.34	-	-	0.29
23031+1856	-	0.58	-	-	0.21
23106+0603	-	0.15	-	-	-
23157+0618	0.42	0.88	-0.09	-	0.46
23161+2457	-	1.14	-	0.87	0.59
23176+2356	0.42	1.10	0.48	0.51	0.39
23179+2702	0.37	0.29	-0.27	0.40	-
23179+1657	0.34	-0.30	-1.16	-	0.44
23201+0805	-	1.34	-	-	0.18
23204+0601	-	1.94	-	-	-
23213+0923	0.25	0.22	-0.60	0.32	-
23252+2318	0.36	0.14	-0.49	0.64	-
23254+0830	-	1.38	-	-	0.58
23256+2315	0.44	0.07	-0.36	0.39	-
23259+2208	0.49	0.46	-0.33	0.54	0.53
23262+0314	0.46	0.87	-0.02	0.41	-
23277+1529	-	0.15	-	0.37	0.37
23336+0152	0.61	0.30	-0.43	0.67	-

Table 6—Continued

IRAS Name	rms <sub>1667,1665</sub> (mJy)	$\log \frac{L_{\text{OH}}^{\text{pred}}}{L_{\odot}}$	$\log \frac{L_{\text{OH}}^{\text{max}}}{L_{\odot}}$	rms <sub>1612</sub> (mJy)	rms <sub>1720</sub> (mJy)
(1)	(2)	(3)	(4)	(5)	(6)
23381+2654	-	1.04	-	0.21	0.18
23387+2516	-	1.22	-	-	0.28
23410+0228	-	2.18	-	0.24	-
23414+0014	-	0.96	-	-	0.33
23433+1147	0.45	0.22	-0.19	0.50	-
23446+1519	-	0.98	-	-	0.34
23456+2056	-	0.76	-	-	0.26
23471+2939	0.59	0.33	0.08	0.29	0.39
23485+1952	-	0.84	-	0.38	-
23488+1949	-	1.34	-	1.31	-
23488+2018	-	1.45	-	0.46	0.42
23532+2513	-	1.58	-	-	-
23560+1026	-	0.51	-	0.26	0.44
23564+1833	-	0.35	-	0.44	0.52
23568+2028	0.45	-0.21	-0.69	-	-
23587+1249	-	0.23	-	0.34	0.52
23591+2312	-	0.69	-	0.45	-
23594+3622	-	1.32	-	1.35	1.33
23597+1241	0.32	0.57	-0.12	0.29	0.35

Table 7. The Mean and Median H I mass values within different  $L_{\text{IR}}$  ranges

IR Luminosity ( $L_{\odot}$ )	$L_{\text{IR}} \leq 10^{10.49}$	$10^{10.50} \leq L_{\text{IR}} \leq 10^{10.99}$	$10^{11.00} \leq L_{\text{IR}} \leq 10^{11.49}$	$L_{\text{IR}} \geq 10^{11.50}$
Mean H I mass	$10^{9.29 \pm 0.10}$	$10^{9.67 \pm 0.07}$	$10^{9.69 \pm 0.08}$	$10^{9.99 \pm 0.10}$
Median H I mass	$10^{9.19}$	$10^{9.72}$	$10^{9.78}$	$10^{9.86}$

Table 8a. The occurrence of H I 21 cm absorption in galaxies within different  $L_{\text{IR}}$  ranges

IR Luminosity ( $L_{\odot}$ )	$L_{\text{IR}} \leq 10^{10.49}$	$10^{10.50} \leq L_{\text{IR}} \leq 10^{10.99}$	$10^{11.00} \leq L_{\text{IR}} \leq 10^{11.49}$	$L_{\text{IR}} \geq 10^{11.50}$
No. (abs. or abs.+emis.)	0	2	3	5
Total No. of galaxies	10	32	29	13
% with Absorption	0%	6.25%	10.3%	38.5%

Table 8b. NVSS flux density distribution of the galaxies with H I absorption within different  $L_{\text{IR}}$  ranges

IR Luminosity ( $L_{\odot}$ )	$L_{\text{IR}} \leq 10^{10.49}$	$10^{10.50} \leq L_{\text{IR}} \leq 10^{10.99}$	$10^{11.00} \leq L_{\text{IR}} \leq 10^{11.49}$	$L_{\text{IR}} \geq 10^{11.50}$
Median NVSS Flux (mJy)	20.40	24.15	31.5	15.8
Mean NVSS Flux (mJy)	$48.33 \pm 20.27$	$37.52 \pm 6.26$	$36.6 \pm 5.92$	$47.33 \pm 19.43$
Mean Flux with abs (mJy)	-	28.9	82.33	90.22

Table 9. The occurrence of OH 18 cm main line (absorption or emission) in galaxies within different  $L_{\text{IR}}$  ranges

IR Luminosity ( $L_{\odot}$ )	$L_{\text{IR}} \leq 10^{10.49}$	$10^{10.50} \leq L_{\text{IR}} \leq 10^{10.99}$	$10^{11.00} \leq L_{\text{IR}} \leq 10^{11.49}$	$L_{\text{IR}} \geq 10^{11.50}$
No. (abs. or emis.)	0	2	0	5
Total No. of galaxies	9	19	5	6
% OH Detections	0%	10.5%	0%	83.3%